PHENOTYPING RODENT MODELS OF OBESITY USING MAGNETIC RESONANCE IMAGING

BY

DAVID HERBERT JOHNSON

Submitted in partial fulfillment of the requirements
For the degree of Doctor of Philosophy

Dissertation adviser: David L. Wilson, PhD

DEPARTMENT OF BIOMEDICAL ENGINEERING
CASE WESTERN RESERVE UNIVERSITY

January 2010

CASE WESTERN RESERVE UNIVERSITY

SCHOOL OF GRADUATE STUDIES

We hereby approve the thesis/dissertation of

_____David Herbert Johnson_____

candidate for the _____Ph.D._____degree *.

(signed)_____David L. Wilson_____

     (chair of the committee)

     _____Christopher A. Flask_____

     _____Xin Yu_____

     _____Joseph H. Nadeau_____

     _____

     _____

(date) _____May 22, 2009_____

*We also certify that written approval has been obtained for any proprietary material

contained therein.

This dissertation is dedicated to my wife, Lyn, who supported me throughout the years. Я тебя люблю, Дорогая.

Table of Contents

List of Figures

Acknowledgements

Thank you to my advisor and committee who guided me through my graduate studies. I could never have imagined the long journey from start to finish in my Ph.D., but now I cannot imagine being satisfied with any less.

List of Abbreviations

1D   One dimensional

2D   Two dimensional

3D   Three dimensional

3PD   Three Point Dixon

ADC   Analog to Digital Converter

BMI   Body Mass Index

CHESS   Chemical Shift Selective

CNR   Contrast to Noise Ratio

CPU   Central Processor Unit

CT   Computed Tomography

CUDA   Compute Unified Device Architecture

DEXA   Dual-Energy X-Ray Absorptiometry

DSC   Dice Similarity Coefficient

DICOM   Digital Imaging and Communications in Medicine

FLASH   Fast Low Angle SHot

GPU   graphics processor unit

H&E   Hematoxylin and Eosin

HU   Hounsfeld units

IDEAL   Iterative Decomposition and Echo Asymmetry with Least squares estimation

FOV   Field of view

MR   Magnetic Resonance

MRI   Magnetic Resonance Imaging

NASH Non-alcoholic steatohepatitis

ORO Oil red O

RARE Rapid Acquisition with Relaxation Enhancement

ROI Region of Interest

SNR Signal to Noise Ratio

SIMD Single Instruction, Multiple Data

T1 Longitudinal relaxation time

T1-W T1-weighted

T2 Transverse relaxation time

T2-W T2-weighted

T2* Transverse relaxation time for gradient echo acquisitions

TE Echo time

TG Triglyceride

TR Repetition time

US Ultrasound

PHENOTYPING RODENT MODELS OF OBESITY USING MAGNETIC RESONANCE IMAGING

Abstract

DAVID HERBERT JOHNSON

The emergence of dedicated, small animal imaging systems provides an excellent opportunity to study obesity using the rat and mouse models which will be critical to increasing our basic knowledge as well as deriving new treatments. MRI is well suited for quantifying fat depots (e.g., visceral, subcutaneous, hepatic, muscular) and for helping to determine the role of genetic, environmental, and therapeutic factors on lipid accumulation, metabolism, and disease. Assessment of lipid depots is important because of the linkage of visceral and ectopic depots to insulin resistance, vascular disease, etc.

The importance of making reproducible imaging measurements can never be underestimated when conducting a study of many animals, and we demonstrated that ratio imaging enables reliable quantification even on a human clinical 1.5T MRI scanner. Scan-rescan variability and intra-operator variability were each reduced to a 2% coefficient of variation or less when the semi-automatic ratio image analysis was used. Receiver coil signal intensity inhomogeneity of over 200% across the field of view was flattened to less than 3% variation by ratio imaging. Using the SHR/SHROB rat model of dietary and genetic obesity, we found a novel image phenotype which showed that visceral adipose tissue depots are increased in both genetic and dietary obesity, but subcutaneous adipose tissue is uniquely linked to dietary obesity, at least in this model.

A method for robust fat-water reconstruction was developed on a small animal, high field scanner, where field inhomogeneity is far worse than on a clinical scanner. Severe field inhomogeneity was corrected by adapting the Iterative Decomposition and Echo Asymmetry with Least squares estimation (IDEAL) to the high field scanner. IDEAL reconstruction time was reduced by 50% when a graphics card was used in calculating a novel, vectorized form of the IDEAL equations. The reconstruction was also improved by applying *a priori* constraints to the linear extrapolation and fitting of the field inhomogeneity parameter, which removed error propagation across the image.

MRI phenotypes were identified and validated on the high field scanner using an important, well-established mouse model of dietary obesity. C57BL/6J mice on high and low fat diets were imaged using the new IDEAL technique, and the semi-automatic ratio image analysis was used to show significant differences in visceral and subcutaneous adipose tissue volumes. High fat diet mice had significantly higher concentrations of liver lipids than the low fat diet mice whether measured by IDEAL (P=0.002) or by a chemical assay (P<0.001). In contrast to IDEAL, CHESS measurements failed to detect reliable differences in either tissue volumes or liver fat content, demonstrating the clear superiority of the IDEAL technique for phenotyping mice on the high field scanner.

Chapter 1   Introduction

1.1   Obesity

Obesity has reached epidemic proportions, and it is associated with many serious medical conditions, including high blood pressure, diabetes, heart disease, stroke, gallbladder disease and cancer of the liver, breast, prostate, and colon. Obesity has been shown to have a substantial negative effect on longevity, reducing the length of life of severely obese people by an estimated 5 to 20 years (1). In fact, despite a 1,000 year trend of increasing life expectancy, Olshansky et al. predict that obesity might actually reduce life expectancy in the US in coming years (2). In short, obesity is rapidly becoming perhaps the major health concern in our society today.

It has long been observed that persons with an android (apple) body shape are at greater risk to develop cardiovascular disease than those with a gynoid (pear) body shape (3,4). More recently, this observation has been related to visceral versus subcutaneous adipose tissue, with the presence of visceral adipose tissue being related to diseases such as insulin resistance, type II diabetes, and cardiovascular disease (5). Visceral fat is frequently associated with impairment of glucose and lipid metabolism, and even in non-obese humans, it is correlated with metabolic risk factors for insulin resistance, elevated blood lipids, and heart disease (6). More recent studies are highlighting a relationship between specific fat depots and metabolic syndrome. Fat accumulation outside of adipose tissue is correlated with deleterious metabolic effects. These ectopic depots include muscle and liver, and accumulation of fat in cells of the liver and muscles has been linked to insulin resistance (7,8). The mechanism is not well understood, but measuring lipid concentration in liver and muscle could provide early insight into these key metabolic

tissues. Currently, diagnosis of type II diabetes is based on the fasting blood glucose level, but this may be observed later than the accumulation of ectopic lipid (7).

MRI can uniquely measure both the volume of adipose tissues and the concentration in ectopic fat depots, which could be important diagnostic targets. Rodents provide a unique opportunity to study effects of genes and controlled environments on obesity, insulin resistance, and diabetes (9). We compared lean spontaneously hypertensive rats (SHRs) on a chow diet, dietary obese SHRs on a high fat, high sucrose diet, and genetically obese SHROB on a chow diet. We also compared C57BL/6J mice on high and low fat diets. Together, these cohorts provide an opportunity to compare genetically obese and dietary obese rodents with lean controls.

1.2   *Genetic Factors and the Metabolic Syndrome*

Genetic influences on obesity are complex, and investigators are studying a variety of genetically modified mouse and rat models which are either prone or resistant to obesity. Obesity-related genes have been explored using chromosome substitution strains so as to identify the genes which influence the development of obesity (10). Chromosome substitution strains can easily create 100's of different genetic mouse strains to examine the genetic factors involved in lipid metabolism. A fast lipid distribution imaging workup is critical to identifying significantly different mouse strains and screening candidate obesity genes. Our target MRI acquisition time is greatly reduced, giving us a throughput sufficient to use MR as a standard phenotyping measurement for gene discovery. In addition, a full lipid work up would be most helpful in evaluation of diet, drugs, and other interventions for diabetes and obesity. For example, it was conjectured that orlistat, a reversible inhibitor of gastric and pancreatic

lipase which blocks absorption of approximately 30% of dietary triglycerides, might have special benefit in fatty liver accumulation and NASH. However, this was not born out in a recent study, which used liver biopsy for assessment (11). With our technology, future preclinical studies can routinely include depot-selective data, a capability that may help assess drug action (12).

Currently the following four clinical abnormalities are the criteria for diagnosis of Metabolic Syndrome: obesity (body mass index (BMI) > 30 kg/m2), non-insulin dependent diabetes mellitus (fasting glucose > 100 mg/dL), hypertension (blood pressure > 130/85 mm Hg), and hyperinsulinemia (elevated fasting insulin). It is difficult to establish cause and effect, but it has been observed that weight reduction can improve glycemic control, reduce blood pressure, and reduce cholesterol levels (13). The HERITAGE epidemiological study implicated visceral fat as a risk factor independent of total body fat (14). Note that a newer definition of obesity (waist circumference above 40 inches in men and 35 inches in women) was created to be a surrogate for measuring visceral adipose tissue (15). More recent studies are highlighting a relationship between specific fat depots and metabolic syndrome. Fat accumulation outside of adipose tissue is correlated with deleterious metabolic effects, which motivates the use of imaging techniques.

1.3 Imaging of Obesity

Not only is obesity significant, the role of imaging in obesity is also significant. MRI can unambiguously follow lipid accumulation/depletion in depots (visceral, subcutaneous, muscle, liver, etc.). As compared to biopsy/dissection and biochemical analyses, MRI has the advantage of being non-invasive and less biased from tissue

sampling. There are clear connections between lipid accumulation in various depots and complications. For example, it has long been observed that visceral fat is "worse" than subcutaneous fat with regards to development of diabetes, cardiovascular disease, etc. Emerging evidence suggests that the ectopic fat depots are even more closely linked to complications; e.g., lipid accumulation in muscle and liver is a leading indicator for diabetes and metabolic syndrome (16,17). There are definite genetic linkages to fat distribution (18-20).

In preclinical animals, MRI is favored over the traditional method of dissection, due to the excellent fat-water contrast, sensitivity, and reproducibility (21). Fat tissue volume measured by MRI correlates well with tissue wet weight determined by gross dissection (22-24). Tang et al. performed a longitudinal study of obese and aging rats and found that both MRI and dissection accurately assessed changes in adipose tissue, liver, and skeletal muscle weight (25). However they found that MRI systematically underestimates dissection whole body weight by 6%, which they attribute to the absence of the tail and hair weights (up to 3%). They note that acquiring thinner slices brings the weight estimated by MRI closer to that of dissection, which supports the hypothesis that the underestimation may be instead due to the partial volume effect, an imaging artifact caused by anisotropic voxels. Ballester et al. established that this artifact may cause an underestimation of volumes by 20-60% in brain images (26). The effect on adipose tissue volume is unknown, but ectopic fat depots share the irregular shape and high surface area of brain structures (e.g. white matter).

Many groups have used in vivo imaging techniques to probe lipid metabolism in specific animal models of obesity and diabetes (22,27-33). However, the majority of

these studies have provided only a single imaging assessment such as total adipose tissue content or intra-myocellular lipid content. Very few, if any, studies have been conducted that provide a more comprehensive array of lipid assessments including adipose tissue compartmental volumes and ectopic lipid fractions with the aim of providing a more complete phenotyping of animal strains. The biggest resistance to performing these studies has been the expensive nature of imaging in general and concerns about the reproducibility of the measurements. We overcame this limitation by developing the fundamental imaging and analysis techniques that in combination provide a rapid and robust characterization of adipose tissue and ectopic fat stores in mice and rats.

1.4   *CT, X-Ray, and Ultrasound Applied to Obesity*

Computed Tomography (CT) and Dual-Energy X-Ray Absorptiometry (DEXA) are two other modalities for assessing whole body fat depots. CT has been used in many studies of human obesity, but fewer studies have investigated CT imaging of obese rodents. The main advantage of using CT is that the signal intensity is directly related to the attenuation coefficient in Hounsfeld units (HU). After calibration, CT images can be reproducibly thresholded due to the lower attenuation of fat (-190 to -30 HU) as compared to skeletal muscle (30 to 100 HU, (34)). Janssen et al. measured visceral adipose tissue in both black and white humans using CT and reported standard errors ranging from 2.3 to 8.0 cm^2, in agreement with body mass index and waist circumference (35). Reductions in CT adipose tissue volume measurements were found to correlate well with reductions in body mass index and waist circumference after a 20 week exercise program. Coefficients of variation in CT-based measurements of adipose tissue volumes are smaller than MRI-based measurements, possibly due to the shorter acquisition time

and thus reduction in motion artifacts (36). Ross et al. showed that MRI volumes correlate well with CT volumes in rats (37). The CT signal intensity can also be used to quantify the concentration of fat in ectopic depots (e.g. liver and muscle) assuming a linearity intensity values from mixing of the fat and water tissue classes. Disadvantages of CT include exposure to ionizing radiation, which may impact longitudinal studies.

Dual-Energy X-Ray Absorptiometry (DEXA) is a form of projection X-ray imaging where images are acquired using both a high energy beam and low energy beam. The primary application of DEXA is in measuring bone mineral density by subtracting the two images (34). Body composition analysis (e.g. fat concentration in skeletal muscles) is possible by using different energy levels to maximize fat-water contrast. The radiation exposure is much lower than CT imaging because only one projection is typically acquired. Unfortunately, DEXA is limited by the single projection acquired. A number of assumptions about body composition (e.g. bone mass and other calibration parameters) are required to model the image intensities, and subjects with widely varying body thicknesses may result in inaccurate measurements.

Ultrasound (US) and anthropomorphic measurements are also used in studying obesity, but there are significant challenges associated with them. The main advantage of these techniques is that the cost is much lower than CT or MRI scans. Unfortunately, applications to whole body fat assessment are limited. Skin calipers cannot accurately measure very thick fat folds, such as those found in obese patients, and the combination of anthropomorphic measurements has limited value in predicting visceral and subcutaneous adipose tissue volumes (34). Ultrasound has the advantage of being able to measure the thickness of most skin depots, but the fat-water contrast in the images is poor

due to the only slight differences in acoustic impedance between adipose tissue and muscles. Interpretation of speckle patterns is required to distinguish tissues, which is not a reliable operation even among trained users (34). A study of morbidly obese humans before and 1 year after bariatric surgery found that ultrasound was only weakly correlated with CT visceral adipose tissue area (R^2=0.38) (38). A further challenge is the limited depth of penetration, which must be traded off against the resolution of the image because higher frequency waves do not penetrate as deeply into tissue. This problem is exacerbated when studying rodents instead of humans, as a nearly 10X increase in frequency is required to obtain equivalent anatomical resolution, but depth of penetration is reduced correspondingly. A recently developed ultrasound system for mice can obtain very high resolution images (57 μm x 57 μm x 40 μm) when operating at 40 MHz, but the focal depth is only 6 mm (39). The carrier frequency and thus image resolution must be significantly reduced to reach any posterior anatomical structures, and even then the presence of any air (e.g. the lungs) will prevent the signal echoes from returning to the transducer. The inaccuracies in ultrasound and anthropomorphic measurements prevent these modalities from making significant contributions to obesity research.

1.5   MRI Applied to Obesity

MRI has a number of advantages for studying obesity. One important advantage is that no ionizing radiation is necessary to acquire images, unlike CT or X-Ray. But MRI is also well-known for better soft tissue contrast than other modalities (34). Fat has a much shorter longitudinal relaxation time (T1) than most other tissues, and endogenous contrast between adipose tissue and most other tissues in MR images can therefore be created simply by using a short repetition time (TR) (40). A variety of additional

acquisition strategies unique to MRI can be used to enhance fat-water contrast (41). A preparation of inverting the signal magnetization prior to acquisition can be used to provide fat-water contrast via manipulating the delay between inversion and acquisition. Contrast is based on the longitudinal relaxation time, and either fat or water can be nearly eliminated from the image. Unfortunately, inversion recovery increases the minimum acquisition time and unnecessarily reduces SNR in the images because eliminating one species will necessary also reduce the signal in the other from overlap in the fat and water recovery curves.

Instead of utilizing T1 differences between fat and water, their distinct precession frequencies can be used to create contrast. Chemical shift selective (CHESS) pulses can be used to apply an off-resonance excitation and spoiling to remove fat signals (42,43). Alternatively, the CHESS pulse can be on-resonance to remove the water signal. While this technique works well when the main field is well-shimmed, it fails outside the shimmed volume and also in locations of field inhomogeneity due to anatomical structures (e.g. air-tissue interfaces). The main concern of using CHESS pulses is the likelihood of failure even inside a single image, which limits the circumstances under which they can be considered useful for quantitative measurements. These failures can be addressed by separating fat and water on the basis of the measured phase in each pixel, as described by Dixon (44). Many phase-based mathematical models require at least one additional image to estimate and remove the field inhomogeneity artifact (45), but the additional scanner time can used to increase the SNR of the estimated fat and water images. Adoption of Dixon-like models has been slowed due to the complexity and

unreliability of reconstruction algorithms, especially the requirement for phase unwrapping.

A number of image artifacts must be addressed to make quantitative measurements. Group comparisons in an animal study are not reliable without addressing a number of MRI artifacts that affect quantification. One example is that the image signal intensity varies in the image with the distance to the receiver coil, which is frequently referred to as a bias field. Signal intensity bias fields confound the post-processing image analysis used to measure volumes. For example, a threshold may be used to separate fat from water in T1-weighted images. Taking the ratio of two images is the best solution for canceling the bias field artifacts in MRI, and we investigated the beneficial effects of ratio imaging on scan-rescan reproducibility, intra-operator image segmentation variability, T1 and T2 corrections, and partial volume effects. Previous studies in human and rodent obesity have not addressed all of these artifacts or their reduction via ratio imaging.

Another major problem is the chemical shift artifact, which confounds quantitative analysis of gray level values in MR images because the fat and water signals are spatially misaligned (i.e. shifted). The shift can be predicted by MR physics and removed in post-processing via image registration. The current trend in MRI is to increase SNR by using higher field strength magnets. The chemical shift artifact becomes worse on these high field scanners, and therefore post-processing corrections become even more important. An even bigger problem is that the main field (B0) becomes much more inhomogeneous on high field scanners, which motivates the development of robust

B0 correction algorithms. Even after B0 inhomogeneity has been removed, it is still important to correct the other image artifacts to produce robust measurements.

The effects of these artifacts can be expressed in an equation for the signal intensity based on the solution to the Bloch equations for the spin echo experiment. At the coordinates (x,y), the signal intensity in the unsaturated image (I_{FW}) has fat and water spin densities ($\rho_{0,F}$ and $\rho_{0,W}$), T1 and T2 relaxation effects for both water and fat (T1F, T2F, T1W, and T2W), and a spatially varying receiver coil sensitivity pattern, or bias field (Λ). The fat and water spin densities are misaligned along the frequency encoding axis (x) due to the chemical shift. Using the coordinate system of the fat signal as a reference, the water signal is uniformly shift along the frequency encoding axis by Δx pixels.

$$I_{FW}(x,y) = \Lambda(x,y) \cdot \rho_{0,F}(x,y)(1-e^{-TR/T1F})e^{-TE/T2F} + \Lambda(x+\Delta x,y) \cdot \rho_{0,W}(x+\Delta x,y)(1-e^{-TR/T1W})e^{-TE/T2W} \quad (1.1)$$

If the fat and water components could be measured separately, the T1 and T2 relaxation effects could be removed and image analysis could proceed from Eq. (1.1). However, the bias field (Λ) would still confound the analysis of signal intensities. Instead of relying on just one image, the ratio of two images can be used to cancel the bias field as well as enable quantitative analysis.

1.5.1   Fat-water Separation Techniques

The principal acquisition strategies for generating ratio images are CHEmical Shift Selective imaging (CHESS) (43), the IDEAL (Iterative Decomposition and Echo Asymmetry with Least squares estimation) method (46-51), Multi-Point Dixon (MPD) methods (45,52) and spectral excitation techniques (42,43). The MPD techniques are

typically implemented in rapid imaging schema such as steady state pulse sequence (53,54) which can dramatically reduce the time to acquire the data sets required to generate separate fat and water images. More importantly, various image reconstruction methods have also been developed to correct for variation in the main magnetic field, which can be extremely deleterious on high field MRI scanners (55). These corrections are a significant advantage over spectral excitation techniques and are essential for accurate quantification of lipid volumes.

The Dixon methods and IDEAL require the acquisition of images with several distinct fat-water phase differences. A mathematical model for the relative phase between fat and water is used to estimate each component, and a B0 correction may also be included. For example, the 3-point Dixon (3PD) method acquires two images with the same fat-water phase to estimate ΔB0 and an additional image where fat and water have opposing phases (Figure 1-1). In comparison, IDEAL uses three equally spaced but asymmetric echo times about the unit circle which maximize the SNR of the final fat and water estimates (47). The IDEAL method is also distinct from Dixon methods because the observed signals are fitted in a least-squares sense rather than using an analytical solution of equations.

Figure 1-1. 3 Point Dixon vs. 3-Point IDEAL

3PT Dixon	3PT IDEAL
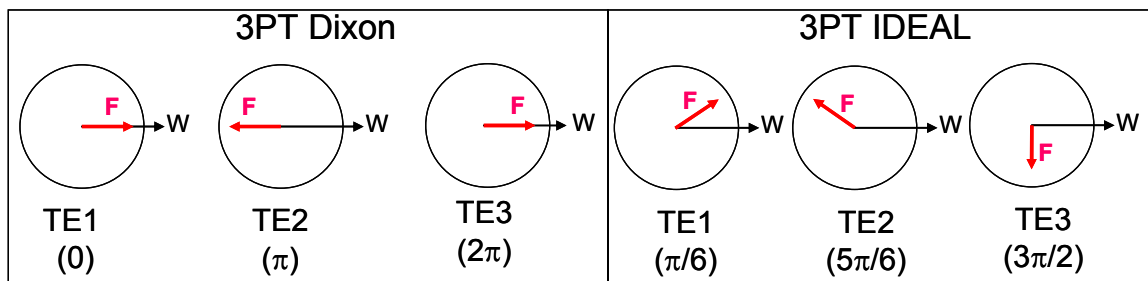
A comparison of different acquisition 3-point fat-water estimation techniques. The 3-point IDEAL technique uses a combination of asymmetric echo times for SNR efficiency, whereas the 3-point Dixon method uses symmetric echo times to make formulating the underlying equations simpler.

Both of these methods perform a B0 correction, but IDEAL does not use phase unwrapping, which is a difficult and error-prone operation. Research on phase unwrapping has been performed for over 20 years, and yet no general, reliable solution is available for MRI (56). In contrast, a number of solutions for making accurate IDEAL reconstructions have been explored. Generally, the correct solution will have a smooth B0 map. Region growing with linear extrapolation is one technique that can solve some images (48). Downsampling has been used to reduce the effect of image noise on finding the correct solution (51). Exhaustive evaluation of a discrete set of possible solutions in each pixel using a Markov-Random Field to reward smoothness is another potential answer (57). There is still room for improvement among all these techniques, especially when the B0 inhomogeneity undergoes rapid spatial changes.

1.6 General Purpose Computing on Graphics Cards

IDEAL is a robust fat-water reconstruction technique, but it is computationally expensive because three or more TEs are acquired, tripling the data to be processed. Datasets can easily reach hundreds of megabytes, and the processing time can be 20 minutes or longer in some implementations (e.g. Matlab). However, the reconstruction algorithm is fundamentally the same in each pixel, which implies that the operations can

be carried out in parallel. This type of data-parallel reconstruction is appropriate for using the highly parallel graphics processor unit (GPU). The Nvidia CUDA architecture makes it possible to realize highly parallel algorithms on commodity graphics cards, which may have hundreds of individual processor units with fast memory access speeds. Other MRI reconstruction algorithms, e.g. SENSE, have recently been shown to be much faster when implemented on graphics hardware (58). Non-Cartesian reconstructions have been speed up on the GPU by a factor of 21 (59). The speed advantages of using a GPU will become more important as the trend towards higher resolution images continues to produce larger MRI datasets, and we showed that significant speed increases are possible for the IDEAL algorithm when vectorized math and a GPU are utilized.

1.7   Overview of the Dissertation

This dissertation focuses on developing MRI techniques for practical studies of obese rats and mice. The specific aims, one per chapter, address concrete problems. The final chapter provides conclusions and a discussion of possible future work.

1.7.1   Semi-automatic Ratio Image Analysis

Chapter 2 explores the use of a clinical human scanner and CHESS imaging in studying a group of obese rats. The semi-automatic image segmentation algorithm developed in this chapter forms the basis for ratio image analysis, a critical technique for conducting reproducible rodent MRI experiments. Bias field, T1, T2, and partial volume effects are characterized and corrected. Scan-rescan variability and intra-observer variability are demonstrated to be acceptable when ratio imaging is used. Distinct MRI

phenotypes are identified in the rats and associated with dietary obesity and genetic obesity.

1.7.2 Robust Fat-Water Reconstruction on a Graphics Card

Chapter 3 demonstrates a number of improvements to IDEAL reconstruction. The IDEAL equations are vectorized and implemented on a commodity graphics card. Reconstruction time on the GPU is decreased to 50% of CPU-only reconstruction time. Brent's method is applied to the IDEAL reconstruction, and a reduced number of function evaluations are required to solve almost every pixel in the image as compared to golden section search. The linear extrapolation of field inhomogeneity is shown to be much more robust when the slope of the 2D fit is restricted to avoid propagating errors throughout the image.

1.7.3 IDEAL Mouse Imaging on a High Field Scanner

Chapter 4 extends semi-automatic image segmentation algorithm to high field, small animal MRI and IDEAL imaging instead of CHESS imaging. The robust IDEAL method of Chapter 3 is applied to an experiment with a well-known mouse model of dietary obesity. MRI phenotypes are validated and compared to body weight, histology, and chemical lipid extraction. Oil/water phantom experiments are used to validate T1 and T2 corrections in the IDEAL framework.

1.7.4 Conclusions and Future Work

Chapter 5 summarizes the results and provides a discussion of possible extensions of the work. New opportunities are discussed in the context of the current work.

Chapter 2   Semi-automatic Ratio Image Analysis

2.1   Background

A clinical 1.5T MRI scanner can be used to phenotype obese rodents, and there are a number of good reasons to investigate the use of a low field scanner. Not every research center has access to a high field, small animal scanner, and thus there are more opportunities to perform routine animal studies on a clinical scanner. The field inhomogeneity is less of a problem when the field of view for a rat or mouse is less because the scanner is homogeneous over a much larger volume. Relaxivity constants (e.g. T1, T2) are well known at 1.5T, and corrections for T1 and T2 variations have been explored on 1.5T systems before (42,60). Finally and most importantly, the analysis of ratio images developed on a low field scanner will also be applicable to ratio images acquired on a high field scanner. Many artifacts are common to both high and low field scanners, and post-processing techniques can be reused when extending the methods from a low field scanner to a high field scanner.

When planning a study of rodent obesity, there are several MRI-specific artifacts that confound MRI measurements and increase errors. Receiver coil sensitivity inhomogeneity is a problem with whole body imaging, which is needed to measure the entire subcutaneous and visceral fat depots. The spatial non-uniformity of the receiver coil confounds image analysis when a threshold is used to separate fat from water in T1-weighted images. The choice of the threshold should be derived to avoid picking a different threshold in each dataset. An operator will need to trace the abdominal cavity to separate the visceral adipose tissue depot, and variations between multiple operators should be minimized to increase the reproducibility of this technique. The ratio of two

images can cancel the receiver coil sensitivity inhomogeneity and enable robust and semi-automatic processing.

We present an image acquisition and analysis method which eliminates technical limitations including the signal intensity bias field, spatial chemical shift artifact, and operator bias due to thresholding. Our semi-automatic algorithm enables rapid phenotypic analysis of rat MRI images by acquiring two co-registered image sets followed by image processing and parameter estimation to correct these artifacts. The only difference between the two images sets is the selective suppression of the water signal, which is deliberately spoiled by the use of CHemical Shift Selective (CHESS) pulses (43). Volumes of adipose tissues and other organs are computed after manual segmentation of the abdominal wall and image classification by thresholding. The intensity values in the ratio image are used to correct partial volume effects.

We use MRI to assess visceral and subcutaneous fat for genetically obese SHROB rats and dietary obese SHR rats as compared to lean SHR control rats. We first report theoretical aspects of ratio imaging with a mathematical model for the signal intensity in the ratio image. This is followed by the semi-automatic image segmentation algorithm developed to measure volumes of subcutaneous and visceral adipose tissue. We next present the results of applying this methodology to a study of genetic and dietary obesity. Finally, we discuss the advantages and tradeoffs of ratio imaging.

2.2 *Methods and Materials*

2.2.1 Theory

We solved the Bloch equations for the signal intensity in both the water-saturated and unsaturated images and developed a model for the signal intensity in the ratio image. At the coordinates (x,y), the signal intensity in the unsaturated image (I_{FW}) has fat and water spin densities ($\rho_{0,F}$ and $\rho_{0,W}$), T1 and T2 relaxation effects for both water and fat (T1F, T2F, T1W, and T2W), and a spatially varying receiver coil sensitivity pattern, or bias field (Λ). We assumed that saturated lipid protons dominate the fat signal and neglect unsaturated lipid protons.

$$I_{FW}(x,y) = \Lambda(x,y) \cdot \rho_{0,F}(x,y)(1 - e^{-TR/T1F})e^{-TE/T2F} + \Lambda(x+\Delta x, y) \cdot \rho_{0,W}(x+\Delta x, y)(1 - e^{-TR/T1W})e^{-TE/T2W} \quad (2.1)$$

The fat and water spin densities are misaligned along the frequency encoding axis (x) due to the chemical shift. Using the coordinate system of the fat signal as a reference, the water signal is uniformly shifted along the frequency encoding axis by Δx pixels. The theoretical shift was given by a calculation using the receiver bandwidth (*BW*), the on-resonance frequency of water (γB_0), and the spectral separation between fat and water (3.35 ppm) (61).

$$\Delta x = \frac{\gamma B_0 \cdot 3.35\text{ppm}}{BW} \quad (2.2)$$

Assuming that all water spins are saturated with the CHESS pulse, the model for the intensity in the water-saturated image was I_F.

$$I_F(x,y) = \Lambda(x,y) \cdot \rho_{0,F}(x,y)(1 - e^{-TR/T1F})e^{-TE/T2F} \quad (2.3)$$

The spin density of fat was found from Eq. (2.3) by dividing the fat only image by the fat relaxation terms taken from the literature (T1F = 250 ms, T2F = 60 ms) (61).

$$\Lambda(x,y) \cdot \rho_{0,F}(x,y) = \frac{I_F(x,y)}{(1-e^{-TR/T1F})e^{-TE/T2F}} \quad (2.4)$$

The spin density of water was found by subtracting Eq. (2.3) from Eq. (2.1) and dividing by the water relaxation terms (T1W = 900 ms, T2W = 50 ms) (61).

$$\Lambda(x+\Delta x,y) \cdot \rho_{0,W}(x+\Delta x,y) = \frac{I_{FW}(x,y)-I_F(x,y)}{(1-e^{-TR/T1W})e^{-TE/T2W}} \quad (2.5)$$

A ratio image (I_r) was produced from dividing the fat spin density (Eq. (2.4)) by the total spin density (Eq. (2.4) + Eq. (2.5)). The water spin density was shifted Δx pixels by interpolation in the x axis. The bias field (Λ) was canceled by taking the ratio.

$$I_r(x,y) = \frac{\rho_{0,F}(x,y)}{\rho_{0,F}(x,y)+\rho_{0,W}(x,y)} = \frac{\frac{I_F(x,y)}{[(1-e^{-TR/T1F})e^{-TE/T2F}]}}{\frac{I_F(x,y)}{[(1-e^{-TR/T1F})e^{-TE/T2F}]}+\frac{I_{FW}(x,y)-I_F(x,y)}{(1-e^{-TR/T1W})e^{-TE/T2W}}} \quad (2.6)$$

2.2.2   MRI Acquisitions.

Two separate but co-registered image sets were acquired on a Siemens Sonata 1.5T MRI scanner. T1-weighted spin echo images (TR/TE = 1240/13 ms, matrix = 256x96x29 to 256x144x30, FOV = 200x82.5x58 to 220x123.75x60 mm, adjusted for rat size) were acquired with and without CHESS water suppression to generate both "fat+water" and "fat-only" image sets. The body coil was used for both RF transmit and receive for phantoms; a human head coil was used on rat studies. We did a specific experiment to test the ability of this methodology to eliminate large bias fields. A custom-made two-channel phased array coil (4" I.D.) was used with one array disabled to create a strong signal intensity variation for one dataset. A reduced receiver bandwidth of 90 Hz/voxel was used to improve SNR and induce chemical shift artifacts. Four averages

were used to minimize respiratory artifacts in the absence of respiratory gating for rodents on the clinical scanner.

Phantom Imaging Studies. To validate our ratio imaging method, images of a 3L plastic bottle filled with half soybean oil and half deionized water were created. The dynamic range of signal intensities in the ratio image was tested by rotating the oil-water meniscus in a rotated sagittal slice, which created a partial volume effect (as before except FOV=319x159.5x20 mm, matrix = 128x64x20, BW = 300 Hz/voxel, 10 averages). A line profile of signal intensity in the ratio image was plotted along the meniscus. Three adjacent columns were averaged to improve the SNR.

Animal Experiments. To test the effectiveness of this new methodology, we evaluated the genetically obese spontaneously hypertensive rat (SHROB (62)) in comparison to SHR lean littermate controls. Comparisons of the genetically obese rats (SHROB) to dietary obese rats (SHR-DO) provide new insights into metabolic syndrome when compared against a control of SHR on a normal diet. Commonly summarized as metabolic syndrome, the overlapping conditions of hypertension, obesity, insulin resistance, and physical inactivity all increase risk of cardiovascular heart disease (63). SHROB rats provide a striking model for metabolic syndrome in humans because it develops all of these conditions (64). We investigated the effects of diet and genetics on visceral and subcutaneous obesity, which are important diagnostic and therapeutic targets (65). Animal studies were conducted under a protocol approved by the Institutional Animal Care and Use Committee at Case Western Reserve University.

To test the biological application of this technique, we chose a variety of ages and body weights among twelve genetically obese SHROB, six dietary obese SHR-DO, and

six non-obese SHR. Animals were scanned using the imaging protocol described above. The rats were anesthetized by 1.0-2.5% isoflurane and restrained within a rat-sized tube. Voxel sizes varied from 0.78x0.78x2mm to 0.86x0.86x2mm because the field of view had to be increased for the more obese rats.

Measurement Reproducibility. We designed experiments to evaluate the variability of image acquisition and image analysis on adipose tissue quantification. Image analysis variability was assessed by comparing results from different operators on the same rodent images. Six operators measured visceral and subcutaneous adipose tissue volumes on a subset of animals using our software. Operators traced the abdominal cavity in all 28 slices of a SHROB water-suppressed dataset, saved the result, and then picked a threshold in the T1W image to separate muscles and other organs from adipose tissues. Tracing the abdominal cavity took approximately 25-35 minutes after a brief training session on a separate dataset. All datasets were processed in the semi-automatic ratio image analysis program (see below, Image Analysis and Visualization). Volumes of adipose tissues were computed both with user-chosen thresholds and alternatively with the semi-automatic image processing. Volume overlap fractions were calculated for each operator relative to the expert operator, who reviewed all of the segmentations and also segmented all of the other data sets.

We quantified the degree of similarity between operators before and after the semi-automatic ratio image analysis method using the Dice Similarity Coefficient (DSC)

$$DSC(A,B) = 2\frac{|A \cap B|}{|A| + |B|} \tag{2.7}$$

The DSC measures the overlap between two sets, A and B, relative to their total size (66). A DSC above 0.7 indicates good agreement at least in some applications such

as psychological testing, and the maximum possible DSC of 1 indicates perfect agreement (67). We used the expert operator's segmentation as the ground truth (A) and computed DSC's for each of the five other operators (B) against it.

A scan-rescan-rescan experiment was used to quantify instrumental and analysis variability in volume measurements. In a single session, a SHROB was scanned three times and repositioned each time between scans. The MRI scanner was allowed to run its internal calibrations (i.e. shimming and adjustment of Fourier Gain) each time. A single expert operator analyzed the images using the semi-automatic ratio image analysis program. Statistics were calculated using a test that corrects for the multiple comparison penalty (Tukey's Honestly Significant Difference) in a freely available statistics package (the R Project for Statistical Computing (68)). P values below 0.05 were considered significant.

IMAGE ANALYSIS AND VISUALIZATION

We now describe the implementation of the semi-automatic ratio image analysis method, used to quantify volumes of adipose tissue depots. Briefly, the image analysis consisted of finding the appropriate alignment of the water signal with respect to the fat signal using image registration followed by calculation of the theoretical model for the signal intensity in the ratio image. The background air pixels were removed using morphological operations, and a label image was created to map each of the tissues (i.e. visceral adipose tissue, subcutaneous adipose tissue, and muscle/other organs). Partial volumes were corrected for each tissue type. Signal intensities were compared by manually placing small ROIs in the liver, muscle, adipose tissue, and kidneys in the ratio

images. Volume rendering was used to visually compare adipose tissue in different groups of rats.

Image Registration. The misalignment of the fat and water signals was corrected using image registration. The exact shift depends on the combination of the off-resonance frequency of fat, receiver bandwidth (as shown in Eq. (2.2)), and macroscopic B_0 field inhomogeneities. We therefore compared the theoretical shift to image registration of the estimated fat and water spin density images. Our initial estimate of the spatial fat water shift (Δx) comes from the scanner's reported bandwidth and on-resonance frequency, which are recorded in DICOM tags. We used a receiver bandwidth of 220 Hz/voxel in acquiring all images, which gave a theoretical shift of 2.36 pixels. We found the optimal shift by computing mutual information between the estimated fat and water spin density images (Eq. (3), (4)) at offsets from $+\Delta x$ to $-\Delta x$ pixels by 0.01 pixel steps (Figure 2-1(a)). Linear interpolation was used, and a special CV-LIN correction was applied to prevent so-called "scalloping" artifacts (69). Air pixels, as identified in label images described below, were not considered in calculations. We validated that the chemical shift artifact was due to the off-resonance frequency of fat, not field inhomogeneities. The maximum mutual information occurred at the theoretically predicted value of $+\Delta x$ pixels. It was too slow to repeat the complete search for every dataset; instead the mutual information was calculated only for the theoretical values of $+\Delta x$ and $-\Delta x$ from Eq. (2.2). The offset with the higher mutual information was retained and used for a more accurate and slower piecewise cubic Hermite interpolation before recalculating the ratio image (70). After applying Eq. (2.6), a corrected ratio image (Figure 2-1-c) has sharper edges,

clearer intramuscular fat streaks, and a better delineation of the abdominal wall than that before alignment (Figure 2-1-b).

**Figure 2-1. Chemical shift artifact correction**

(a) (b) (c)
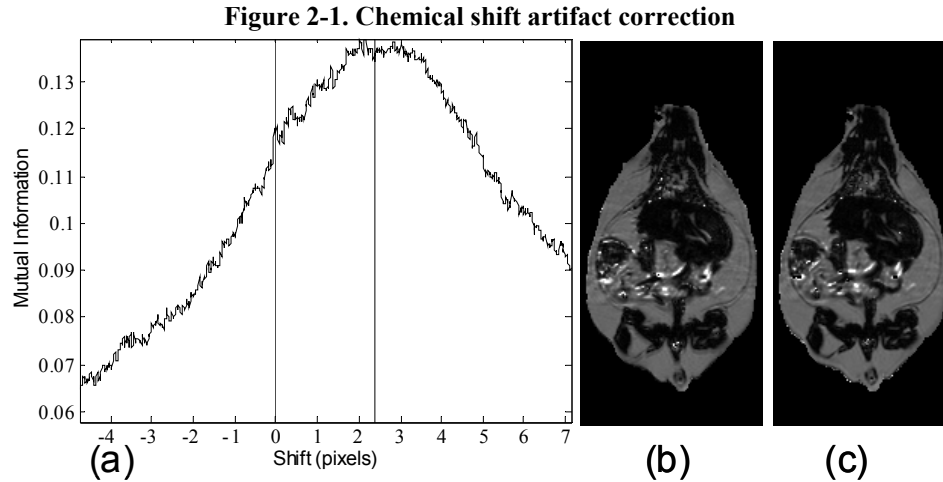
Alignment of the fat-only and water-only signals along the frequency encoding direction restores edges lost to the chemical shift artifact. CV-LIN helps to estimate optimal alignment based on mutual information (a). A large 'scalloping' artifact appears around whole integer shifts when linear interpolation is used. The use of CV-LIN removes the artifact, and the optimal solution becomes apparent at the maximum mutual information. The prediction of the optimal alignment from the MRI equations is shown (a, vertical bars). Visual inspection confirms the prediction of mutual information. The aligned ratio image (c, +2.36 pixel shift) is superior to the unaligned ratio image (b, no shift). Edges at adipose tissue/muscle boundaries are restored around the abdominal wall, and intramuscular fat depots become more apparent.

Semi-automatic Image Segmentation. We expedited the measurement of visceral and subcutaneous adipose tissue by automating it as much as possible. The only manual input was tracing the abdominal cavity in all slices of the water-suppressed dataset using Analyze (AnalyzeDirect, Inc., Overland Park, KS). The segmentation was saved as a label image with regions inside and outside the abdominal wall, which was used later to separate visceral and subcutaneous adipose tissue, respectively. Respiratory motion ghosting artifacts and background noise / air were automatically eliminated by creating a mask image using an in-house Matlab program (The Mathworks Inc., Novi, MI) (Figure 2-2). Four averages were taken in the image acquisition, effectively reducing the ghost signal intensities. Air voxels were removed from all images by measuring the mean and standard deviation of a 10 pixel x 10 pixel background region in a water-only

image (Figure 2-2-c). A global lower bound threshold ($\mu+3\sigma$) was applied to remove air in all slices. This threshold also had the effect of thresholding out some of the weaker ghost artifacts (Figure 2-2-d). Remaining air artifacts were removed using the observation that they tended to occur in random positions between slices. We used a 3D morphological opening on each slice with a 2x2x2 structural element to remove small islands of voxels outside the animal. A morphological closing operation with a 2x2x2 structural element removed small holes inside the animals (Figure 2-2-e). In some instances, there were remaining air artifacts. The body of the rodent was segmented using region growing and any unconnected voxels were deemed to be air. (Figure 2-2-f). In some limited cases it was necessary to manually fix remaining artifacts (Figure 2-2-g). Flood fill algorithms are an alternative approach to fixing holes in the mask images, but we found that a simple manual correction was quick and sufficient. At this point, three regions can be identified: external air, interior to the abdominal wall, and exterior to the abdominal wall.

**Figure 2-2. Semi-automatic ratio image segmentation**
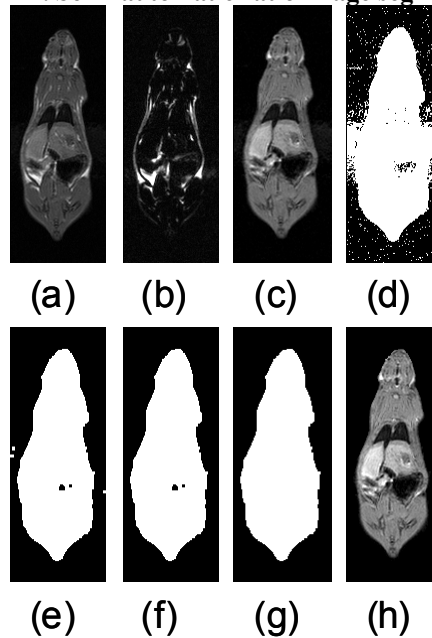
Semi-automatic image processing is used to create a mask. The (fat+water) (a) and fat-only images are transformed into estimates of fat-only and water-only signals as per Eq. 3 and 4 (b, c, resp.). The water-only signal is thresholded to remove air (d). Ghosting artifacts are substantially reduced following morphological opening and closing (e). Disconnected ghosts of high signal are removed by a region growing seeded from the center pixel of the image volume (f). A human observer edits the image map to fix any remaining problems (g). Finally, the mask is applied to the water only signal to show how artifacts have been removed (h).

Ratio images were used to identify adipose tissue using a fixed threshold (see below) or, optionally, a user defined threshold. Voxels above the threshold were labeled adipose tissue in the ratio image (Figure 2-3-a). Voxels inside and outside the abdominal cavity were labeled as visceral or subcutaneous adipose tissue, respectively. In some limited cases it was necessary to manually remove the interior of bones which have a high fat content and can be misclassified. Peristalsis and metal residues in fecal matter in the gastrointestinal tract were eliminated by excluding all voxels in the ratio image with values > 1.0. At this point, we have label images consisting of air; visceral adipose tissue; subcutaneous adipose tissue, including some intramuscular fat streaks; muscles/organs inside the abdominal cavity, and muscles/organs outside the abdominal cavity (Figure 2-3-b). Volumes were computed without partial volume correction by counting the

number of voxels in each label and multiplying by the volume of a single voxel in ml.

Volumes were computed with partial volume correction as described later.

Figure 2-3. Ratio image used for segmentation and partial volume correction
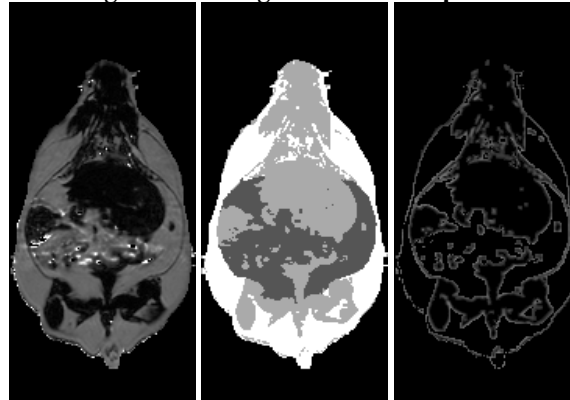
(a)   (b)   (c)

Creation of a label image is used by classification and partial volume correction, shown here in a genetically obese SHROB. The ratio image (a) is classified into four classes showed in (b): subcutaneous adipose tissue (white), and visceral adipose tissue (dark gray), muscle/non-adipose tissues (light gray), and air (black). Partial volume correction is performed both on subcutaneous and visceral adipose tissue separately by finding voxels at the boundaries of tissues. The voxels of (b) affected by 3x3 erosion and dilation are labeled for adipose tissue partial volume correction as shown in (c). An alternative is to correct all the pixels in the rat. The arrow indicates a location where intramuscular fat streaks appear but lack strong edges.

Histograms of ratio values were analyzed to find an optimal threshold for separating adipose tissues from muscles and other organs. Peaks in the ratio histograms were found to be remarkably similar between animals. Gaussians fit to the water and fat peaks had means and standard deviations of 0.05 ± 0.02 and 0.77 ± 0.02, respectively. These distributions were comparable to those in an oil/water phantom (see Results, Figure 2-4). We used a fixed threshold halfway between the peaks at 0.61.

Figure 2-4. Water phantom calibration curve

<center>(a) (b)</center>
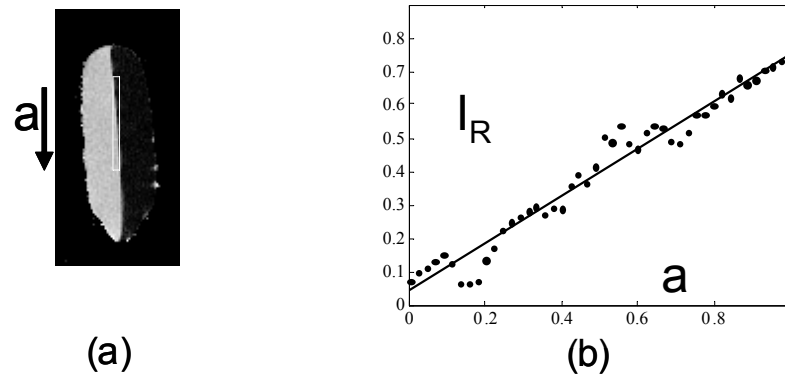
Calibration of ratio calculation on a vegetable oil and deionized water phantom. A line profile (shown as a box in (a)) in a single sagittal slice of the phantom provides a calibration between all-oil and all-water voxels when plotted from top to bottom of the image (b). A linear fit of the data gave $I_R=0.75*\alpha+0.05(1-\alpha)$ with $R^2=0.96$ (P<0.01). Oil and water and signal intensities in the ratio image were 0.75±0.03 and 0.05±0.03, respectively.

Partial Volume Correction. Partial volume errors were corrected two different ways. In the first method, we identified and corrected edge voxels. A border of edge voxels were found by computing the difference between dilation and erosion (3x3 structuring element) of the visceral and subcutaneous adipose labels (Figure 2-3-c). The signal intensity of each voxel in the ratio image (I_R) was modeled as a linear combination weighted by the fraction of adipose tissue in a given voxel (a).

$$I_R = \alpha I_{AT} + (1-\alpha)I_W \tag{2.8}$$

Where I_W and I_{AT} were signal intensities for pure voxels as obtained from the means of Gaussian fits to peaks in the ratio histogram. For the edge voxels, the fraction of adipose tissue (α) was estimated from Eq. 6 using measured I_R values. Volume fractions α and $(1 - \alpha)$ in each edge voxel were added to the volume of adipose tissue and muscle/organs, respectively. The α fraction was added to the visceral or subcutaneous volume depending upon whether the edge voxel was originally inside or outside the abdominal cavity, respectively. The $(1 - \alpha)$ fraction was added to the muscle/organs independent of the abdominal cavity. In the second method, we corrected all voxels in the

animal using the same algorithm. This was advantageous for unmixing partial volumes due to thick slices.

Signal Intensity Comparison. A single operator placed ROI's of 5x5 pixels in 3 consecutive slices of the right side of the liver in the ratio images. For comparison ROI's were also placed in the most uniform regions of muscle in the lower right hindlimb, visceral adipose tissue, and the kidneys. The pixel values were tested for statistically significant differences between lean SHRs, dietary obese SHRs, and genetically obese SHROBs.

Volume Rendering. Because the bias field was removed, ratio images were useful for volume rendering. Volume rendering revealed fat distribution within the animals and was especially useful for identifying fat streaks in the muscle. Ratio images were visualized using a special network script written for volume rendering in Amira (Mercury Computer Systems, Berlin, Germany). Each of the three classes in the label volume was exported separately from Matlab as a series of TIFF files containing the fraction of adipose tissue (α) of 0-1 linearly rescaled to the TIFF range of $1-2^{16}$ before importing into Amira. Each series of TIFF's corresponded to separate volumes for muscles/organs, visceral adipose tissue, and subcutaneous adipose tissue. We linked separate color maps and opacity modules to each image volume for rendering. Color maps were customized to provide contrast between tissues (e.g. different shades of pink for subcutaneous and visceral adipose tissue). Opacity was also adjusted to make muscle more opaque than adipose tissues. Rats were viewed from arbitrary angles using camera rotation and cropping. Adipose tissue distribution and partial volume effects were examined. Intramuscular fat streaks of the rats were compared visually.

2.3　　　*Results*

Ratio Images and Bias Field Correction. Voxel composition, as determined by the ratio model (Eq. (2.6)), was found to be accurate and linear in a phantom of soybean oil and deionized water (Figure 2-4). Signal intensities in the ratio image of water and oil were measured by placing circular ROIs in the image far away from the meniscus. The line profile from pure water to pure oil showed a transition from water (0.05 ± 0.03) to oil (0.75 ± 0.03), which matched the values in the respective ROIs. Ringing artifacts occurred due to limited phase encoding, but a least squares linear regression of signal intensity vs. distance along the line profile was linear with an excellent fit (R^2=0.96, Figure 2-4-b). This distance was directly proportional to the partial volume effect (α, Eq. (2.8)) because the line profile was positioned around the exact beginning and end of the intersection of the meniscus with the image grid.

**Figure 2-5. SHROB/SHR rat ratio signal intensities in liver**
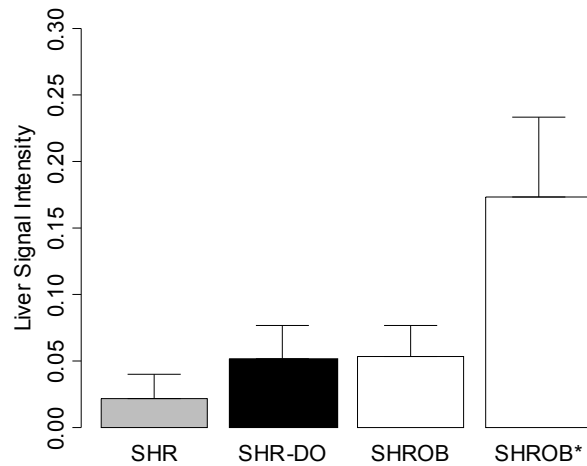
Signal intensities in the liver were consistent with hepatic steatosis, a known disease of this rodent model. ROIs of 5x5 pixels were placed in 3 consecutive slices in each animal in the right side of the liver. Six of the twelve SHROBs (denoted SHROB*) were retrospectively identified as having unusually hyperintense livers. As compared to the other SHROBs, the six SHROB* were not statistically significantly heavier or younger, however they did have more visceral adipose tissue. Signal intensities in the ratio images were statistically significantly different between all groups except SHROB and SHR-DO (P<0.01). Signal intensities in muscle, kidney, and visceral adipose tissue were not different.

Signal intensities in the liver varied greatly between cohorts, and some SHROBS exhibited elevated values consistent with hepatic steatosis, a known disease of this rodent model (62) (Figure 2-5). Lean SHRs had low values (0.01 - 0.04). SHR-DO had slightly higher values (0.03 - 0.08). SHROBs tended to cluster at high (0.12 - 0.24) or low (0.04 - 0.07) liver values, suggesting two phenotypes (SHROB and SHROB*, respectively). As compared to SHROB, the six SHROB* animals had significantly different liver signal intensities (P<0.05). They were not significantly heavier (504.8±46.9 g vs. 438.9±47.3 g, P>0.20) or younger (172.3±28.7 days vs. 201.8±30.8 days, P>0.98). However, they did have more visceral adipose tissue (107.3±16.5 vs. 87.8±3.7 ml, P<0.02). Liver signal intensities in the ratio images were statistically significantly different between all groups (SHR-SHROB, SHR-SHR-DO, SHROB*-SHROB, etc.), except SHROB and SHR-DO (P<0.01). In other tissues, signal intensities in ratio images were very consistent between

all animal groups. Muscle, kidney, and visceral adipose tissue signal intensities were not different, and they generally were very flat across images. Intramuscular adipose tissue appeared in both SHROB and SHR-DO, but rarely in lean SHRs.

Figure 2-6. Bias field cancelation in SHROB rat

(a)   (b)   (c)   (d)
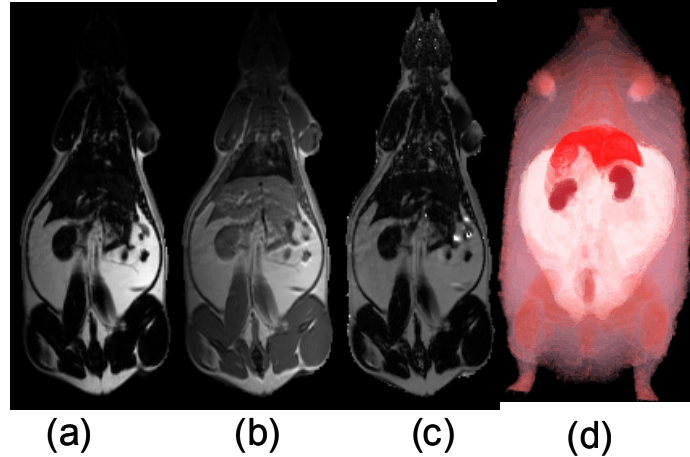
Taking the ratio can also recover datasets which would be otherwise unusable due to coil sensitivity inhomogeneity (a, fat only image and b, fat+water image). Using our method, the 200% left-right bias field in both of the original images is canceled in the ratio image (c). Furthermore, the edges of the abdominal wall are retained. Volume rendering (d) aids in the interpretation of the different amounts of partial volume effects in each type of rat. This SHROB (d) is labeled with color maps for the liver, kidneys, adipose tissue, and other tissues. The ratio values were used for opacity.

This methodology eliminated a large bias field created by a two-channel phased array coil with one array disabled. The left side of the image was over 200% higher than on the right side in both the fat only image (Figure 2-6-a) and fat+water image (Figure 2-6-b) of a SHR-DO. This shared left-right bias field was cancelled in the ratio image (Figure 2-6-c). The edges of the image were preserved and even enhanced by the elimination of the chemical shift artifact. The contrast of the abdominal wall was improved with respect to adjacent adipose tissues especially on the left side of the image. Substantial signal was recovered in the other regions of the image despite severe coil sensitivity drop-off. Volume rendering in a SHROB was greatly aided by the ratio imaging, which eliminates this type of bias field (Figure 2-6-d).

Reproducibility of Measurements and Partial Volume Corrections. Image analysis variability was reduced by the semi-automatic ratio image analysis program (Figure 2-7). Tracings of the abdominal cavity were similar between operators with DSC's of 0.89, 0.91, 0.93, 0.93, and 0.93. Moreover, the final effect of border delineation on adipose tissue volumes is even less because some regions far from adipose tissue borders will not contribute anyway (see below). The thresholds chosen by the operators in the T1W images caused a disagreement about the classification of adipose tissue voxels, as indicated by DSC's after thresholding of 0.76, 0.79, 0.81, 0.86, and 0.91. The different thresholds also caused widely varying measurements of visceral and subcutaneous adipose tissue volume, 54.4±12.6 ml and 68.7±30.6 ml, respectively (Figure 2-7-a).

Figure 2-7. Intra-operator variability and PV correction

(a)   (b)
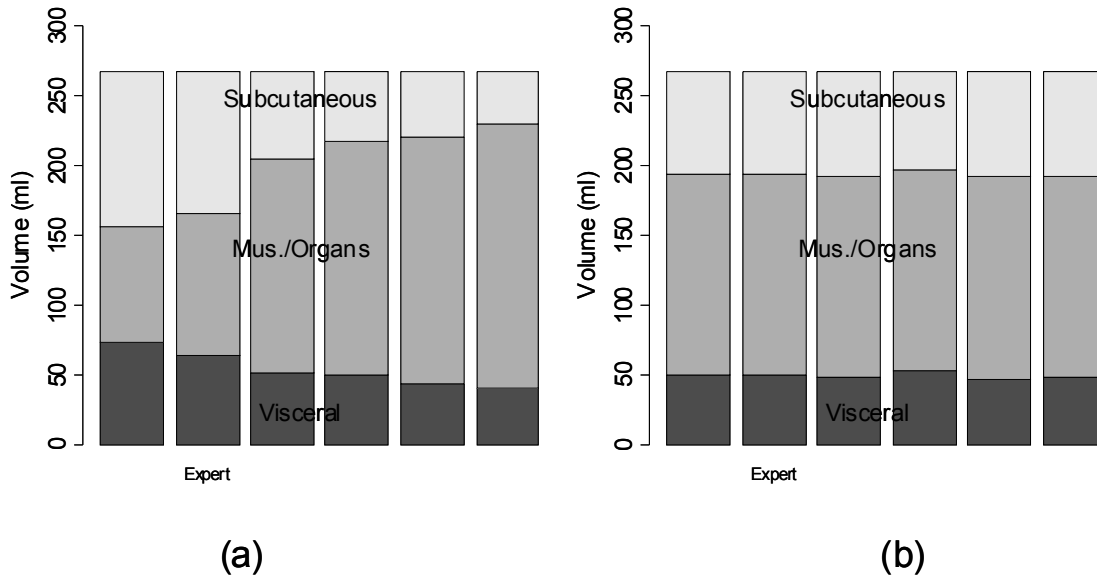
The semi-automatic segmentation was repeated by several human observers on the same data set of a dietary obese SHR (see Figure 2-7). Each observer segmented the abdominal cavity independently. When the volumes of the image were computed by thresholding the T1W image, significantly different volumes were measured by each operator (a). After ratio image calculation and partial volume correction of all pixels in the rat, the differences between observers were substantially reduced (b).

When the semi-automatic ratio image analysis program was run using each of the operator's tracings, the volume measurements became much more consistent (Figure 2-7-b). DSC's improved to 0.96, 0.96, 0.98, 0.98, and 0.99 before applying partial volume correction. Applying partial volume correction on edge voxels gave <1% volume change for each of the 6 analysis volumes. Visceral adipose tissue was 43.9 ± 1.5 ml or 44.0 ± 1.4 ml if only edges were corrected. Subcutaneous adipose tissue was 60.1 ± 1.5 ml before any corrections or 60.6 ± 1.4 ml if only edges were corrected. When we applied partial volume correction to all voxels, the distribution of the 6 measured volumes narrowed and the mean of the 5 moved closer to the expert's values. That is because measurements of visceral and subcutaneous adipose tissue volume became more narrowly distributed, 50.1 ± 1.9 ml and 75.2 ± 1.9 ml, respectively after this correction was applied.

The scan-rescan experiment demonstrated excellent reproducibility and accuracy. When the semi-automated ratio image analysis was used with partial volume correction of all voxels in the rat, measurements of visceral and subcutaneous adipose tissue volumes were remarkably uniform. Visceral adipose tissue volume was 91.2, 87.8, and 90.4 ml for the three measurements, and subcutaneous adipose tissue was 291.1, 288.8, 290.6 ml. Volume measurements of both visceral and subcutaneous adipose tissue were not different, as indicated by the narrow coefficients of variation (i.e. standard deviation divided by mean) of visceral and subcutaneous adipose tissue (2% and 0.5%, respectively). The total volume of the rat was also very reproducible, 472.5, 472.7, and 474.2 ml (Figure 2-8-a). The histograms of each of the positions were practically indistinguishable (Figure 2-8 b-d). We compared the MRI volumes to the weight of the animal on an electronic scale to determine accuracy. Using a standard density for adipose tissue (0.92 g/ml) and other tissues (1.04 g/ml) (25,71), we converted the MRI volumes to weights of 445.5, 446.4, and 447.4 g. These are close to the real body weight determined gravimetrically, 441.7 g. By contrast, a similar analysis prior to partial volume correction of all voxels in the rat produced animal weight estimates of 400.9, 400.5, and 400.5 g, respectively. However, it should be noted that this approximation overestimates total body weight because the volume of the lungs was not excluded. Also, the tail was outside the field of view, so its contribution is not included in the MRI estimates.

Figure 2-8. Scan-rescan and repositioning reproducibility
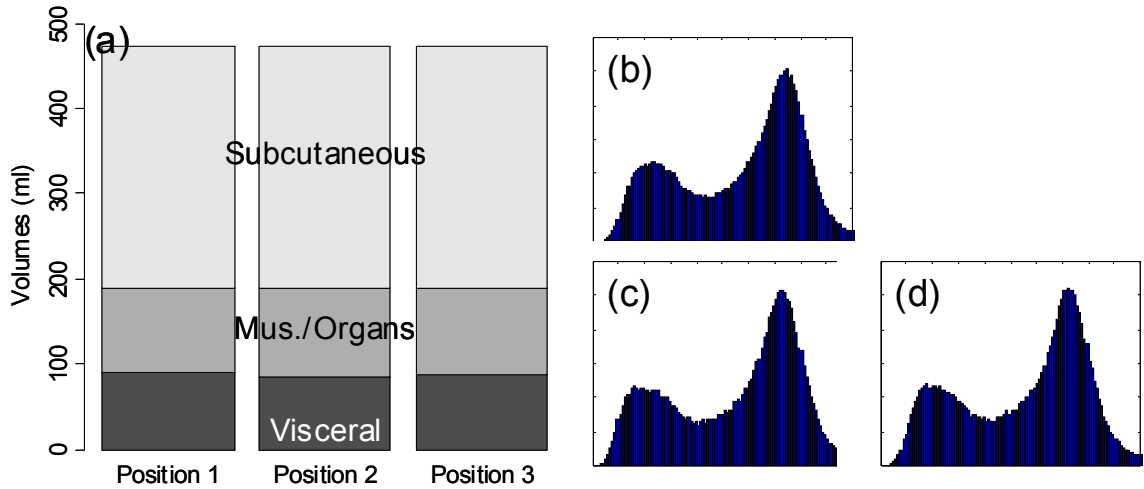
Repositioning a SHROB thrice shows remarkably consistent measures of adipose tissue volumes with a standard error <1% of body volume. Despite physically repositioning the rat on the MRI bed and reshimming the scanner, the tissue volumes (a) and histograms (b-d) varied little. Partial volume correction was performed on all pixels in the rat. The total volume of the animal (the top of the subcutaneous adipose tissue bar) was practically invariant between the scans. Tissue volumes measured in the positions were not significantly different (P > 0.50).

We next analyzed partial volume corrections for all rats using abdominal wall tracings from the single expert operator. Corrections were significant for all rats (Figure 2-9). Partial volume corrections increased visceral adipose tissue volume by 23±2% (SHR), 15±2% (SHR-DO), 12±1% (SHROB) as a percentage of the total volume of visceral adipose tissue. Likewise, average partial volume correction of subcutaneous adipose tissue volumes increased by 26±1% (SHR), 22±2% (SHR-DO), and 13±1% (SHROB). Since the nominal fat volumes varied greatly between lean SHR and SHROB, these corrections varied from 2.3 to 40.7 ml. If we correct just the edge voxels, changes range from 0.2% to 1% of adipose depot volume for these same data sets. Figure 2-3-c shows the location of edge voxels in a SHROB. The biggest relative corrections were in the leaner animals, where muscle and other organs were overestimated in the initial binary segmentation. Generally, most corrections came from intramuscular adipose tissue and as a result of the relatively large slice thickness.

Figure 2-9. PV corrections in SHROB, SHR, and SHR-DO
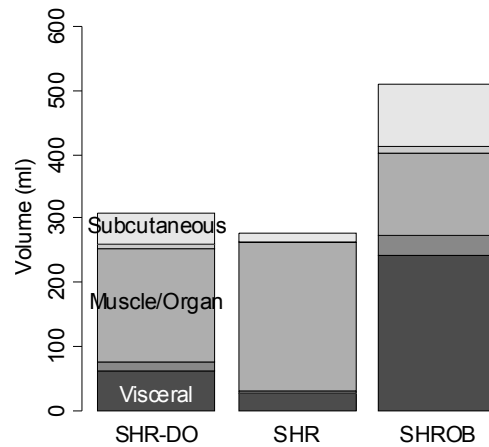
Partial volume corrections differ between types of rats due to the differing adipose distribution. If only the edge pixels are corrected then the overall change in volumes is <1%. However, we found that correcting all the voxels in the rat was significant. The bar plots show each of the depots in ml vs. diet and genetics. The partial volume corrections are shown as gray bars in between the muscle/organ depot and the adipose tissue depots. Generally the amount of correction is proportional to the animal size. The muscle/subcutaneous partial volume effect is smaller in absolute volume, but it is quite large relative to the size of the subcutaneous depot. Partial volume correction enhances the statistical conclusions as described in the text. In every case it was found that the muscle and other organs were over-estimated before partial volume correction.

Genetic/Dietary Obesity Phenotypes. Body composition was very different between lean SHR, and dietary and genetically obese animals (Figure 2-10). Subcutaneous adipose tissue volumes (Figure 2-10-a) were 278.2±42.4 ml (SHROB), 77.3±13.0 ml (SHR-DO), and 33.0±12.6 ml (SHR). Visceral adipose tissue volumes (Figure 2-10-b) were 110.3±17.0 ml (SHROB), 55.9±10.7 ml (SHR-DO), 18.2±5.5 ml (SHR). Subcutaneous adipose tissue volumes were not significantly higher in dietary obesity (P<0.07 SHR-DO vs. SHR) but were highly significantly greater in genetic obesity (P<0.01 SHROB vs. SHR). Visceral adipose tissue volumes were significantly higher in both dietary and genetic obesity (P<0.01 SHR-DO vs. SHR, and P<0.01 SHROB vs. SHR). All differences were several fold greater than the variations measured from the reproducibility measurements above.

Figure 2-10. Subcutaneous and visceral adipose tissue volumes
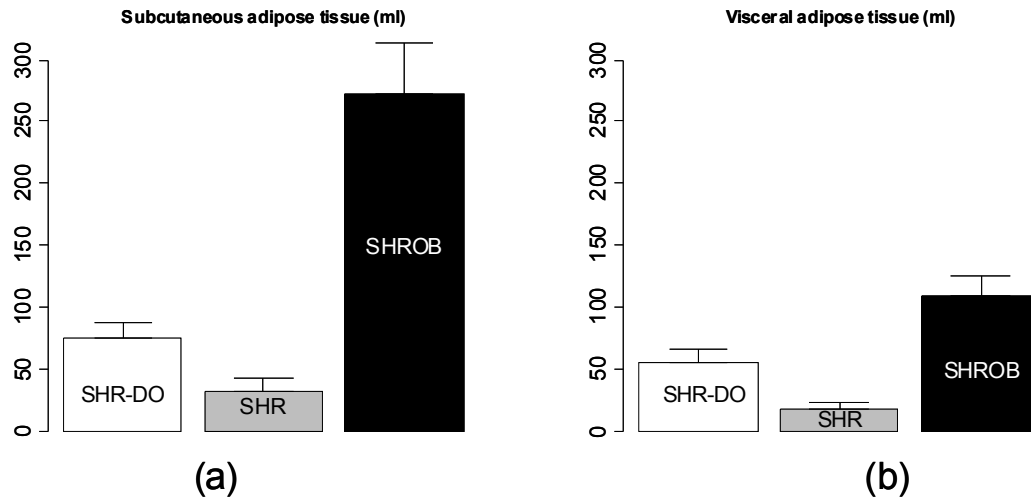
Adipose tissue volumes measured by MRI demonstrate differences in body composition with partial volume correction. The genetic obese SHROB rats (N=12) have significantly higher volumes of visceral (b) and subcutaneous adipose tissue (a) than the dietary obese SHR (N=6) and the lean control SHR rats (N=6). The dietary obese SHR have a significantly higher volume of visceral adipose tissue than the lean control. Subcutaneous adipose tissue was not higher in dietary obese SHR as compared to SHR with or without partial volume correction (P<0.10). Error bars indicate one standard deviation. In all cases the error in the measurement are less than the biological variation, which is much less than the underlying genetic and dietary differences.

Biological and dietary variability was found to be much larger than the measurement errors. For example, the SHROB subcutaneous adipose tissue volume was on average 245.2 ml larger than SHR subcutaneous adipose tissue volume. In comparison, the effect of applying partial volume correction was much smaller (2.7-4.6 ml in SHR, 22.0-40.7 ml in SHROB). Intra-operator variability and repositioning had much smaller effects, as measured by our other methods (1.9 ml and <1 ml, respectively). We concluded that the differences we observed reflect underlying biological differences. It would be interesting to investigate the effects of age and sex in a larger study.

Intramuscular adipose tissue was clearly manifested in the ratio images, and 3D volume visualization aided in locating small "streaks." Volume rendering was useful for visual inspection of fat distribution and the partial volume effect in the rats (Figure 2-6-

d). By manipulating a cropping plane and rotating the view it was possible to appreciate the greater surface area of adipose tissue in lean rats.

2.4 *Discussion*

The ratio image methodology gives a robust, precise measurement of subcutaneous and visceral adipose tissue volumes. Effectively, it allowed us to remove the bias field due to coil sensitivity inhomogeneity and create a robust image analysis approach. In addition, the ratio technique eliminates additional artifacts such as chemical shift misalignment and partial volumes. Providing an estimate of lipid content is an additional bonus. The technique is sufficiently robust that we believe it could be applied robustly across different animals, scanners, coils, and other external factors.

We simplified the ratio image model with assumptions which are valid under our imaging conditions. We assumed that B_0 inhomogeneities were negligible over the rat. Chemical shift-selective excitation techniques are all vulnerable to variations of the main magnetic field, which results in locally inaccurate fat/water suppression. Accurate - shimming reduces overall B_0 variation mitigating the effects of B_0 inhomogeneities. The rat and small phantoms we used are far smaller (<20 cm) than uniform portion of the main field in a clinical scanner (30-40cm), which justifies our assumption. We also neglected RF inhomogeneities (B_1 variation). This is justified by the use of the human head coil for transmit in the animal studies, which is again larger than the rats. These are all reasonable assumptions under our imaging conditions on a clinical scanner.

We tested the sensitivity of the model to small changes in the relaxivity parameters to ensure the results did not vary widely. We reprocessed one SHROB dataset with a variation of +10% to -10% in T1W, T2W, T1F, and T2F, and we recomputed

tissue volumes and ratio image signal intensities. Subcutaneous adipose tissue volume varied from 273.9 to 276.0 ml, less than a 1% change. Visceral adipose tissue volume varied from 93.9 to 96.6 ml, only a 3% change. Muscle/organ volume varied from 117.8 to 122.7 ml, less than a 4% change. The mean signal intensity in the ratio images from 0.78 to 0.81 in visceral adipose tissue, 0.06 to 0.07 in muscle, 0.04 to 0.05 in kidneys, and 0.06 to 0.07 in liver. These signal intensity variations were as small as the variations in the ratio images using the initial relaxivities (e.g. 0.02 standard deviation in liver). We concluded that the model produced consistent results. We assumed that our choice of fat and water relaxivities was adequate for our imaging conditions. This is justified by the short TE, which made the sequence insensitive to T2. Our acquisitions were also somewhat desensitized to T1 by the long TR (i.e. 1200ms).

An alternative to assuming constant relaxivities is to estimate them from MR measurements on a voxel or tissue basis. A relaxometry experiment could be designed to estimate T1 and T2 for each voxel by acquiring multiple echo times and multiple repetition times. Assuming that water and fat are the dominant proton species in each voxel, estimated values could be used in the calculation of the ratio image, Eq. (2.6). Related corrections have been implemented in Iterative Decomposition of water and fat with Echo Asymmetry and Least squares estimation (IDEAL). Liu et al. developed a per-voxel T1 correction based a dual flip angles at the cost of doubling the number of scans required (49). Yu et al. presented a per-voxel T2* correction where the T2* of both fat and water were assumed to be equal due to an injection of Feridex (50). At least in human imaging, iron accumulation in the liver can be a confound for lipid measurements due to T2* effects (72), which suggests that estimation of relaxometry parameters is required for

accurate quantitation. However, voxel estimation of T1 and T2 will necessarily be noisy and depend upon MR artifacts. Ideally, partial volume effects should be considered. Also, our method should be less sensitive to the effects of iron due to the dependence on T2, not T2*. Using average tissue values remains a viable alternative, especially when sensitivities to relaxometry parameters are minimal as argued above.

Our method might not be applicable to high field scanners. At higher field strengths typical for small animal imaging research studies, several artifacts become worse such as B_0 inhomogeneities and chemical shift artifacts. This model can still fix the chemical shift between fat and water, which increases in both Hz and pixels at high field strength. The maximum read-out bandwidth is constrained by gradient strength and the ADC sampling rate, which may be a limiting factor on some scanners (not on preclinical scanners). The tissue relaxitivites change, but T1 and T2 variations can be incorporated into this model with reasonable estimates. The model can also be adapted to a wide variety of pulse sequences / parameters (i.e., FLASH vs. Spin Echo, TR/TE, flip angle, etc.). As it is derived, the model cannot compensate B1 variation, B_0 inhomogeneity, or eddy currents, which are problematic on higher field MRI systems. Fortunately, these types of errors could potentially be compensated for directly with MR acquisition techniques such as adiabatic RF excitation pulses to limit B1 heterogeneity or the use of the Multi-Point Dixon techniques to correct for B_o inhomogeneities.

In its present implementation, a downside is the requirement for two image acquisitions which essentially doubles the overall acquisition time. However, multi-echo acquisitions (73) or alternative trajectories (53) approaches can be utilized to reduce the acquisition time closer to a single acquisition. Another approach is to obtain a single

water-suppressed image and correct any bias field inhomogeneity prior to quantifying fat volumes. One approach is to fit a low-order polynomial to the image and correct the bias field by minimizing image entropy (74,75). Some studies have not corrected the bias field at all (76-78). But, as we have shown here at 1.5T, these effects can be quite significant and can result in lipid quantitation errors as the thresholding/segmentation processes become inaccurate or unreliable.

The three groups of rats provide an interesting contrast between genetic and dietary obesity. Genetically obese SHROBs have a number of metabolic diseases, including severe insulin resistance, glucose intolerance, and hyperlipidemia (29). We found that SHROBs have six times as much visceral adipose tissue and eight times as much subcutaneous adipose tissue as lean control SHRs. In contrast, dietary obese animals (SHR-DOs) have three times the visceral adipose tissue but only twice the subcutaneous adipose tissue of lean control SHRs, and the difference in subcutaneous adipose tissue is not statistically significant. Apparently both diet and genetics are correlated with visceral obesity, but massive expansion of the subcutaneous depot is unique to genetic obesity. Visceral adipose tissue is strongly correlated with metabolic diseases, especially insulin resistance (34). Insulin resistance is apparent in SHROBs with fasting insulin increased to at least 10 times that of SHR littermates while fasting glucose is unchanged (64). Glucose to insulin ratio, an index of insulin resistance, is 9-fold higher in SHROB than SHR. Dietary obese, SHR-DO, animals were comparably insulin resistant to the SHROB animals (9). The increased insulin resistance in the SHR-DO animals correlates well with the increases in visceral depots, which reinforces the link between visceral obesity and insulin resistance (79). It remains an open question whether

subcutaneous adipose tissue is an independent predictor of insulin resistance, but some preliminary studies in humans support this hypothesis (8,80). Bergman et al. observe that metabolic damage and insulin resistance are caused by the storage of lipids outside of visceral adipose tissue (81). The phenotype of SHROBs with elevated visceral adipose tissue and liver fat content is consistent with this "lipid overflow hypothesis."

The results we have shown here demonstrate the importance of partial volume correction for measuring adipose tissue volumes. The primary motivation for partial volume correction in this study was to increase accuracy as well as precision. Voxel anisotropy caused partial volumes to occur because the slices were thicker than the in-plane voxel size. This motivates a partial volume correction to make the data from different animals comparable. The images were acquired at different resolutions due to the different sizes of the animals and constraints of using a clinical scanner. Therefore we corrected partial volume effects in every pixel of the rat to remove this source of variability. It is not surprising that the volumes differ depending on whether all the voxels or just edge voxels were corrected because correcting only the edge voxels leaves a binary segmentation in all non-edge voxels. Alternatives include post-processing corrections, such as Gaussian mixture models and interpolation with reverse diffusion (82).

We have also identified a robust method for calibrating lipid concentration. There are a variety of methods in the literature. Oil-water emulsions are commonly used to make a series of phantoms, but it is difficult to make a stable emulsion over a wide range of oil concentration with the same surfactant, owing to the challenge of stabilizing both oil-in-water and water-in-oil emulsions (42). Further, these emulsions may precipitate

(i.e. break down) over time, which would undermine the reproducibility of a longitudinal study. We chose an alternative approach based on manipulating the partial volume effect. The image acquisition of an unmixed oil-water phantom can be varied to create partial volumes, recreating the portioning of the biological specimen into fat and lean compartments. A thick slice can be shifted across the oil-water meniscus, but this requires many scans (83). Another alterative is to make non-selective projections of oil-water 'wedge' phantoms on the frequency encoding axis, but this requires a custom image reconstruction (84). We modified the method of Hussain et al., who rotated the imaging matrix across the oil-water meniscus to create partial volumes (85). This has proven to be a robust technique which we believe is appropriate for studies where reproducibility is a concern.

Scan-rescan variation gives a general indication of the magnitude of all instrument errors combined with the variability of physically placing the animal in the scanner over a short time. There may be additional instrument variability over a longitudinal experiment. An important aspect was that the animals were positioned casually, and not positioned according to landmarks or placed in a molded frame to lock position. Also, the obese animals were considerably more difficult to position. Our scan-rescan-rescan repositioning experiment showed that the total volume of the rat varied <1.0 ml, which indicates the insensitivity of the analysis algorithm to positioning. This is an important feature for imaging of deformable rodent models. It should be noted that the same operator processed these datasets, which therefore do not include inter-operator variability.

For rapid comparison of animals, we find volume rendering useful. Volume rendering has previously been used to visualize adipose tissue distribution, which has aided studies of obese rodents. Calderan et al. performed a 3D reconstruction of T1-weighted images, which assisted in interpreting anatomical relationships in obese mice (86). They noted the distribution of adipose tissue in an obese rat was predominantly subcutaneous along the caudal aspect of the animal, and the visceral adipose tissue had displaced one of the kidneys. We have also found volume rendering to be useful for examining intramuscular adipose tissue (i.e. "fat streaks") as well as distention of the abdominal cavity. Our ratio imaging methodology works extremely well with volume rendering / classification techniques because of the correction of the bias fields. Large bias fields make volume rendering much harder to interpret because the non-uniform intensity causes confusing intensity variation in the volume renderings.

In conclusion, we have developed a robust imaging and analysis paradigm centered on the generation of ratio images to enable effective phenotyping of rodent models of obesity. The remarkable homogeneity of ratio images is useful for both segmentation and 3D visualization, and reproducibility is also improved. The simplicity and reproducibility of this technique is promising for large scale studies of body composition in obese rodents influenced by diet, genetics, exercise, and drugs. These techniques are also generally applicable to clinical research studies of obesity where it is becoming important to quantify regional lipid distribution to track the effects of diet and exercise interventions (87).

Chapter 3 Robust Fat-Water Reconstruction on a Graphics Card

3.1 Background

Iterative Decomposition and Echo Asymmetry with Least squares estimation (IDEAL) (47) is a robust fat-water reconstruction technique, but it is computationally expensive because three or more TEs are acquired, tripling the data to be processed. Datasets can easily reach hundreds of megabytes, and the processing time can be lengthy. However, the reconstruction algorithm is fundamentally the same in each pixel, which implies that the operations can be carried out in parallel. This type of data-parallel reconstruction is appropriate for using the highly parallel graphics processor unit (GPU). The Nvidia CUDA architecture makes it possible to realize highly parallel algorithms on commodity graphics cards (Figure 3-1). Other MRI reconstruction algorithms, e.g. SENSE, have recently been shown to be much faster when implemented on graphics hardware (58). We investigated the potential speedups in the IDEAL reconstruction when using a GPU, and we made improvements to the reconstruction to make it more suitable for GPU implementation.

Figure 3-1. Nvidia CUDA Architecture
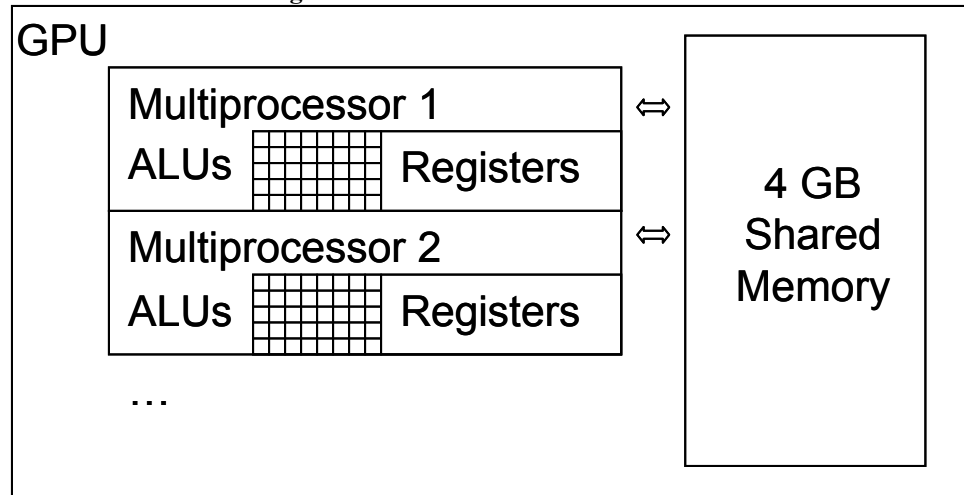
Nvidia CUDA architecture for massively parallel GPU computation. The Quadro FX5800 has 10 SIMT (Single Instruction, Multi-Threaded) multiprocessors, each of which has 24 scalar stream processors running at 400 MHz. Thousands of threads can be simultaneously executed on the multiprocessors, which have a 102 GB/s connection to shared memory. IDEAL is well-suited to SIMT computation because the mathematical operations for reconstruction are identical in each pixel, and the large IDEAL image sets can be stored in the shared memory.

In the present work, we vectorized the IDEAL equations so that they are suitable for massively parallel computation on both GPUs and multicore multithreaded CPU systems. Vectorized equations are also used in a reformulation of Brent's method (88), which provides convergence for the field inhomogeneity parameter (Ψ) with fewer iterations than the current standard of golden section search (51). We demonstrate that vectorized IDEAL scales well from small datasets to large ones when using GPUs and multithreaded CPUs. We also improve the robustness of the linear extrapolation model of Ψ to avoid propagated errors.

3.1.1 Theory

The IDEAL reconstruction has been published in detail elsewhere (47). Here we describe only the vectorization modifications needed to enable massively parallel computation and the histogram analysis of Ψ on a high field scanner. We also modify Brent's Method (88) for parallel computation. The key observation is that the observation

matrix A is spatially independent, and the IDEAL calculations can be rewritten as simple, efficient matrix operations (i.e., vectorized).

The original form of the IDEAL estimator is to solve Eq. (3.1) on a per-pixel basis. As described by Reeder et al. (46), the measured signals S(x,y,TE1) through S(x,y,TE3) are fit in a least squares sense to the observation matrix A to determine the fat and water components p_W and p_F. The field inhomogeneity parameter $\Psi(x,y)$ is initialized to zero and then iteratively varied until the residuals of Eq. (3.1) are minimized. The pseudo-inverse of the observation matrix A is used to determine the fat and water components p_W and p_F.

$$
\underbrace{\begin{bmatrix} S(x,y,TE1) \\ S(x,y,TE2) \\ S(x,y,TE3) \end{bmatrix}}_{S(x,y)} \underbrace{\begin{bmatrix} e^{-j2\pi\psi(x,y)TE1} & 0 & 0 \\ 0 & e^{-j2\pi\psi(x,y)TE2} & 0 \\ 0 & 0 & e^{-j2\pi\psi(x,y)TE3} \end{bmatrix}}_{\Psi(x,y)} = \underbrace{\begin{bmatrix} 1 & e^{j2\pi\Delta f TE1} \\ 1 & e^{j2\pi\Delta f TE2} \\ 1 & e^{j2\pi\Delta f TE3} \end{bmatrix}}_{A} \underbrace{\begin{bmatrix} \rho_W(x,y) \\ \rho_F(x,y) \end{bmatrix}}_{\rho(x,y)} \tag{3.1}
$$

3.1.2   Vectorized IDEAL

We use a vectorized form of Eq. (3.1), which eliminates 'FOR' loops and enables GPU calculation. Although the equations below will show the case of three echo times (TEs) and two proton species, the result is quite general. Vectorized math will be even more important on higher resolution datasets with more TEs.

In contrast to other implementations of IDEAL, the entire image is reconstructed simultaneously. The key observation is that the observation matrix A is spatially independent (i.e., the same calculations are performed in each pixel). Massive speedups are possible on the GPU for parallel tasks like this. The implementation is split into two steps described by Eq. (3.2) and (3.3). In Eq. (3.3), the current estimate of Ψ in every pixel is used to form a new matrix temporary matrix T which is free of phase due to Ψ.

Page 61

Note that the '.*' operator has been introduced to indicate a per-element multiplication instead of a standard matrix inner product.

$$\underbrace{\begin{bmatrix} T(x,y,TE_1) & T(x+1,y,TE_1) & \cdots \\ T(x,y,TE_2) & T(x+1,y,TE_2) & \cdots \\ T(x,y,TE_3) & T(x+1,y,TE_3) & \cdots \end{bmatrix}}_{T} = \underbrace{\begin{bmatrix} S(x,y,TE_1) & S(x+1,y,TE_1) & \cdots \\ S(x,y,TE_2) & S(x+1,y,TE_2) & \cdots \\ S(x,y,TE_3) & S(x+1,y,TE_3) & \cdots \end{bmatrix}}_{S} .* \underbrace{\begin{bmatrix} e^{-j2\pi\psi(x,y)TE_1} & e^{-j2\pi\psi(x+1,y)TE_1} & \cdots \\ e^{-j2\pi\psi(x,y)TE_2} & e^{-j2\pi\psi(x+1,y)TE_2} & \cdots \\ e^{-j2\pi\psi(x,y)TE_3} & e^{-j2\pi\psi(x+1,y)TE_3} & \cdots \end{bmatrix}}_{\Psi} \quad (3.2)$$

The matrix T is used to find the fat and water components and the residuals. In Eq. (3.3), the pseudo inverse of the observation matrix ($A^\dagger$) is multiplied by the intermediate matrix T to give the fat and water least squares estimates. Our notation for the inverse operator should be understood in a least squares sense, i.e. $A^\dagger = \left(A^H A\right)^{-1} A^H$ where H denotes the Hermetian transpose.

$$\underbrace{\begin{bmatrix} \rho_W(x,y) & \rho_W(x+1,y) & \cdots \\ \rho_F(x,y) & \rho_F(x+1,y) & \cdots \end{bmatrix}}_{\rho(x,y)} = \underbrace{\begin{bmatrix} 1 & e^{j2\pi\Delta f\,TE_1} \\ 1 & e^{j2\pi\Delta f\,TE_2} \\ 1 & e^{j2\pi\Delta f\,TE_3} \end{bmatrix}^\dagger}_{A^\dagger} \underbrace{\begin{bmatrix} T(x,y,TE_1) & T(x+1,y,TE_1) & \cdots \\ T(x,y,TE_2) & T(x+1,y,TE_2) & \cdots \\ T(x,y,TE_3) & T(x+1,y,TE_3) & \cdots \end{bmatrix}}_{T} \quad (3.3)$$

The residuals R(x,y,TE) are also formed from the intermediate matrix T. In Eq. (3.4) the product of the projection matrix (I-AA†) and the T matrix yields residuals for each echo time in each pixel. The residuals are squared for each echo time in the pixel and then squared.

$$\underbrace{\begin{bmatrix} R(x,y,TE_1) & R(x+1,y,TE_1) & \cdots \\ R(x,y,TE_2) & R(x+1,y,TE_2) & \cdots \\ R(x,y,TE_3) & R(x+1,y,TE_3) & \cdots \end{bmatrix}}_{R(x,y,TE)} = \underbrace{\left(I - \begin{bmatrix} 1 & e^{j2\pi\Delta f\,TE1} \\ 1 & e^{j2\pi\Delta f\,TE2} \\ 1 & e^{j2\pi\Delta f\,TE3} \end{bmatrix} \begin{bmatrix} 1 & e^{j2\pi\Delta f\,TE1} \\ 1 & e^{j2\pi\Delta f\,TE2} \\ 1 & e^{j2\pi\Delta f\,TE3} \end{bmatrix}^\dagger \right)}_{I-AA^\dagger} \underbrace{\begin{bmatrix} T(x,y,TE_1) & T(x+1,y,TE_1) & \cdots \\ T(x,y,TE_2) & T(x+1,y,TE_2) & \cdots \\ T(x,y,TE_3) & T(x+1,y,TE_3) & \cdots \end{bmatrix}}_{T}$$

$$(3.4)$$

Equations (3.2)-(3.4) are now vectorized and easily implemented on a GPU because they are simply matrix multiplications. The sum of squared residuals is

computed from Eq. (3.4) by summing the squares of the real and imaginary components of R(x,y,TE) over TE. The original dataset S, the observation matrix A and the projection matrix (I-AA†) are pre-computed and statically allocated on the GPU to minimize overhead.

One additional speedup is possible because Eq. (3.2)-(3.4) are not square. our matrix multiplication library is faster for big columns than big rows. The number of pixels in the image will be much bigger than the number of TEs or proton species, so the implementation of Eq. (3.2)-(3.4) actually takes the transpose of all of the components before doing the multiplication by using an elementary property of matrix multiplication. In Eq. (3.5) and (3.6), we show two equivalent ways to multiply matrices (N, P) to get the resulting inner product (M).

$$M = NP \hspace{4cm} (3.5)$$

Eq. (3.5) is equivalent to:

$$M^T = P^T N^T \hspace{4cm} (3.6)$$

In our specific matrix multiplication library, Eq. (3.5) is faster than Eq. (3.6), for large datasets. We speculate the speed difference is because Strassen's matrix multiplication algorithm was designed for square matrices, and non-square multiplications require zero padding. This zero padding may be more efficient in our library for the case of having bigger columns than rows. Regardless of the cause, we implemented (3.5) and (3.6) in the transposed form to gain additional speed.

3.1.3 Comparison of Optimization Routines

Brent's method and golden section search were each vectorized and implemented on the GPU. Golden section search has already been used to solve the IDEAL problem by

Lu and Hargreaves (51). Briefly, golden section search maintains four values of ψ: x0, x1, x2, and x3, as described by Press et al. (88). The endpoints x0 and x3 are an outer bracket on the minimum, and the two internal points x1 and x2 are used to maintain the golden ratio between the right and left segments. Given an initial bracket [AX,CX] and an initial guess BX, x0 and x3 are set to AX and CX, respectively, and x1 and x2 are set to BX and a bracket between BX and a golden section between the smaller of the two intervals. The golden section (G, i.e. the new point at which to evaluate ψ) of an interval (A,B) is given by Eq. (3.7).

$$G = A + \frac{3 - \sqrt{5}}{2}(A - B) \tag{3.7}$$

The objective function (F) is evaluated at both x1 and x2 before the main iteration begins. In every iteration, if F(x1) is less than F(x2) then the left interval will be subdivided by a golden section, the right endpoint will be moved to the left, and the objective function will be evaluated at the new point which is at the golden ratio of the new left bracket. If F(x1) is greater than F(x2) then the right interval is evaluated instead. The algorithm terminates when the width of the outer bracket is small enough (i.e. |x0-x3| is less than the maximum acceptable error tolerance, ε), and the solution for ψ is returned as the smaller of the function values most recently evaluated at x1 and x2.

Vectorization of golden section search is straightforward because x0, x1, x2, and x3 can be turned into column vectors with one entry in the vector for each pixel being solved. Operations on x0, x1, x2, and x3 can be performed with vector math and logical indexing. For example, the termination criterion of |x0-x3|<ε can be accomplished as the vector subtraction of x0 and x3, followed by disregarding the sign of the outcome and comparing each value with the scalar ε. Let DONE be the list of pixels that pass the test,

and NOTDONE be the list of pixels which fail it. The vectorized golden section search algorithm needs to continue iterating upon the pixels in the NOTDONE list, whereas it can stop evaluations in the DONE list. The algorithm terminates when the NOTDONE list becomes empty (i.e. all pixels have achieved the minimum error tolerance). These list operations motivate the name logical indexing because these two lists replace one IF/ELSE statement. Entries in the list can only be either true or false, and there is exactly one entry in the list for each pixel being solved. All of the other IF statements and other conditions in the algorithm are replaced by similar sets of lists. For example, another set of lists is used to keep track of whether F(x1) or F(x2) was smaller in every pixel, and the algorithm explores the golden section in the appropriate interval as described above. The right hand side of Eq. (3.4) is formed from the pixels in the NOTDONE list, so no redundant function evaluations need to be performed in pixels which have already converged. The vectorized golden section search should be at least as fast or faster as a purely FOR-loop based implementation because the vector operations can take advantage of single instruction, multiple data (SIMD) instructions, which are integrated into to recent CPUs.

Brent's method combines inverse quadratic interpolation with golden section search because the former has quadratic convergence, whereas the latter has only linear convergence (88). Brent's method is a completely different algorithm than golden section search for finding minima. For a well-behaved function, the fitted parabola can "jump" to the solution with fewer function evaluations than golden section search. The minimum x value (apex) of the parabola passing through the points (AX, F(AX)), (BX, F(BX)), and (CX,F(CX)) is given by:

$$X = \frac{1}{2} \frac{F(AX).*(BX^2 - CX^2) + F(BX).*(CX^2 - AX^2) + F(CX).*(AX^2 - BX^2)}{F(AX).*(BX - CX) + F(BX).*(CX - AX) + F(CX).*(AX - BX)} \quad (3.8)$$

Brent's method can be summarized as follows. Like golden section search, an initial bracket [AX,CX] and an initial guess BX must be given. Brent's method maintains values of ψ used for fitting the parabola between the best three points most recently evaluated (x,v,w) as well as the value of the residuals at these points (fx,fv,fw). An outer bracket [AX,CX] is also maintained with two additional values of ψ (x1, x2) needed when golden sections are taken instead of parabolic steps. The parabolic interpolation is rejected if the apex lies outside the bracket [AX,CX], in which case the golden section step is taken instead. The outer bracket is reduced every time the objective function is successfully reduced by either the parabolic interpolation or the golden section step. Brent's method also keeps track of the last two steps which were actually taken (DX, EX), and a golden section step is forced whenever the second to last step (EX) would provide no new information about the function by being smaller than the maximum acceptable error tolerance, ε. Golden section steps are also forced when the current step is within ε of the last point evaluated or outer brackets because this also does not provide new information. Convergence is guaranteed by the slow but reliable golden section steps, but the parabolic interpolation is used whenever allowed by the above criteria.

Vectorization of Brent's method is more complicated to implement than golden section search, but the basic ideas remain the same. All of the internal variables of the algorithm are replaced by column vectors, and logical indexing is used in place of the various tests. There are many more logical indexing operations needed to replace all of the IF statements which enforce the criteria for deciding whether to take the parabolic or golden step. The arithmetic operations of Eq. (3.8) should be understood as a per-element

operations carried out in parallel on the GPU despite the fact that AX, BX, etc. are actually huge vectors. The .* operator has been added to emphasize this fact. The cost of evaluating both Eq. (3.7) and (3.8) in every unsolved pixel is much less than the other logical tests to needed by the algorithms to determine which value of ψ should actually be tested. Therefore, both Eq. (3.7) and (3.8) are always evaluated, and then the appropriate values of ψ are chosen per-pixel by the optimization routine based on the logical indexing inside the algorithm.

3.1.4 Disambiguation of ψ by Planar Extrapolation

After one solution for ψ is found in each pixel there remains the problem that there will always exist another value of ψ in the pixel which is also a minimum in the residuals curve but it approximately interchanges ("flips") the estimated fat and water components (48). This is the fundamental fat-water ambiguity in ψ, and the "flipped" value of ψ can be numerically predicted. Consider a pixel which only contains water which has a magnitude of 1 (W=1, F=0). The signal measured in the pixel S(TE) can be described by Eq. (3.9).

$$S(TE) = W \exp(j2\pi\psi TE) \tag{3.9}$$

However, an equivalent signal can be measured if the pixel contains only fat (W=0, F=1) and a different value of ψ is used. Consider $\psi 1 = \psi + \Delta f$ as substituted into Eq. (3.10).

$$
\begin{aligned}
S(TE) &= (F\exp(j2\pi\Delta fTE))\exp(j2\pi\psi 1TE) \\
&= (F\exp(j2\pi\Delta fTE))\exp(j2\pi(\psi - \Delta f)TE) \\
&= F\exp(j2\pi\psi TE)
\end{aligned}
\tag{3.10}
$$

The form of the final line of Eq. (3.10) is equivalent to (3.9) if fat and water are interchanged. Therefore in pixels containing only one proton species there is an intrinsic ambiguity between a solution of ψ where water is the dominant proton species and an equally valid solution where fat is the dominant proton species. Herein the solution of ψ which makes water the dominant species will be referred to as ψ_W, and the equivalent solution for inverting the fat and water estimates will be referred to as ψ_F. It can further be shown that there will always be two possible solutions (ψ_W, ψ_F) even if the voxel contains both proton species. The exact form of the two equivalent solutions is given by Yu et al. as follows (48). The value of ψ which inverts the two proton species (ψ_a) is given as a function of the current value of ψ (ψ_t), the current estimates of fat and water (F, W), and the echo shift chosen by the choice of TEs (ΔTE) in Eq (3.11).

$$\psi_a = \psi_t + \frac{1}{2\pi\Delta TE} \arg\left(\frac{W + F\exp(j2\pi\Delta fTE)}{F + W\exp(j2\pi\Delta fTE)} \right) \tag{3.11}$$

For a pixel which is dominated by one proton species, the difference between ψ_a and ψ_t is approximately equal to Δf. This ambiguity is fundamental to the formulation of the IDEAL method. An equivalent ambiguity can be shown in the 3-point Dixon method when the difference of two in-phase echoes at different TEs is used to estimate $\Delta B0$. By definition, $\psi = \gamma\Delta B0$, and a very similar argument can be constructed using Eq. (3.9)-(3.11). It is impossible to know *a priori* which solution of (ψ_W, ψ_F) is the correct one in a single pixel (56). Instead, the correct solution must be derived using constraints of spatial smoothness between pixels.

A further problem is that the residuals given from the least squares solution are also periodic as derived by Lu et al. (51). Consider the residuals J from a given value of ψ

applied to a set of three signals S(TE1), S(TE2), S(TE3) with a constant spacing of ΔTE used to create the observation matrix A and pseudoinverse A† in Eq (3.12).

$$J(\psi) = \left\| (I - AA\dagger) \begin{bmatrix} \exp(-j2\pi\psi TE1) & 0 & 0 \\ 0 & \exp(-j2\pi\psi TE2) & 0 \\ 0 & 0 & \exp(-j2\pi\psi TE3) \end{bmatrix} \begin{bmatrix} S(TE1) \\ S(TE2) \\ S(TE3) \end{bmatrix} \right\|$$

(3.12)

The choice of equally spaced echoes is beneficial to SNR of the estimated fat and water signals, but it has an unfortunate side-effect in making J periodic. Consider that Eq. (3.12) can be rewritten as follows in Eq without changing J.

$$J(\psi) = \left\| (I - AA\dagger) \begin{bmatrix} 1 & 0 & 0 \\ 0 & \exp(-j2\pi\psi\Delta TE) & 0 \\ 0 & 0 & \exp(-j2\pi\psi(2\Delta TE)) \end{bmatrix} \begin{bmatrix} S(TE1) \\ S(TE2) \\ S(TE3) \end{bmatrix} \right\| \left\| \exp(-j2\pi\psi TE1) \right\|$$

$$= \left\| (I - AA\dagger) \begin{bmatrix} 1 & 0 & 0 \\ 0 & \exp(-j2\pi\psi\Delta TE) & 0 \\ 0 & 0 & \exp(-j2\pi\psi(2\Delta TE)) \end{bmatrix} \begin{bmatrix} S(TE1) \\ S(TE2) \\ S(TE3) \end{bmatrix} \right\|$$

$$= \left\| (I - AA\dagger) \begin{bmatrix} 1 & 0 & 0 \\ 0 & \exp(-j2\pi(\psi + 1/\Delta TE)\Delta TE) & 0 \\ 0 & 0 & \exp(-j2\pi(\psi + 1/\Delta TE)(2\Delta TE)) \end{bmatrix} \begin{bmatrix} S(TE1) \\ S(TE2) \\ S(TE3) \end{bmatrix} \right\|$$

$$= J(\psi + 1/\Delta TE)$$

(3.13)

This periodicity occurs at predict 1/ΔTE intervals, which means that the two possible solutions (ψ_W, ψ_F) discussed above are actually repeated at (ψ_W+N/ΔTE, ψ_F+N/ΔTE) and for any integer N. As previously stated, it is not possible to know *a priori* which of the aliased copies of (ψ_W, ψ_F) is the correct one in any given pixel, and therefore the enforcing spatial smoothness is the only practical solution to the problem.

One successful technique for finding the right value of ψ among the fat-water ambiguous values and their aliases is to use a region growing operation seeded either manually or automatically where the ground truth value of ψ is known or given by an operator (48). Adjacent pixels to the seed are linearly extrapolated from the known region using a square-spiral trajectory through the image. The linear extrapolation can be weighted by the intensities of the original input image data to reduce the effect that air voxels have on the extrapolation (48). Given a neighborhood of solved pixels at $(x(1,1),y(1,1),\ldots)$ with unambiguously solved fat-water solutions $(\psi(1,1), \psi(2,1)\ldots)$, the slope along both x and y (ψ_x, ψ_y) as well as an average value over the neighborhood ψ_0 are estimated in a least-squares sense:

$$W\begin{bmatrix} \psi(1,1) \\ \psi(2,1) \\ \psi(3,1) \\ \vdots \end{bmatrix} = W\begin{bmatrix} x(1,1) & y(1,1) & 1 \\ x(2,1) & y(2,1) & 1 \\ x(3,1) & y(3,1) & 1 \\ \vdots & \vdots & \vdots \end{bmatrix}\begin{bmatrix} \psi_x \\ \psi_y \\ \psi_0 \end{bmatrix} \tag{3.14}$$

where W is a weighting matrix formed from the intensities of the input images where w(i,j) equals the magnitude of the image measured at the first TE:

$$W = \begin{bmatrix} w(1,1) & 0 & 0 & \cdots \\ 0 & w(2,1) & 0 & \cdots \\ 0 & 0 & w(3,1) & \cdots \\ \vdots & \vdots & \vdots & \ddots \end{bmatrix} \tag{3.15}$$

The slopes and offsets are estimated from the weighted least-squares solution to Eq. (3.14). Then the slopes and offsets are used to predict the correct value of ψ at the current X,Y pixel, and the minimum absolute difference between ψ_W, ψ_F and their aliases is chosen as the correct value for $\psi(x,y)$. For example, consider the image shown in Figure 3-2.

Figure 3-2. Planar extrapolation of ψ
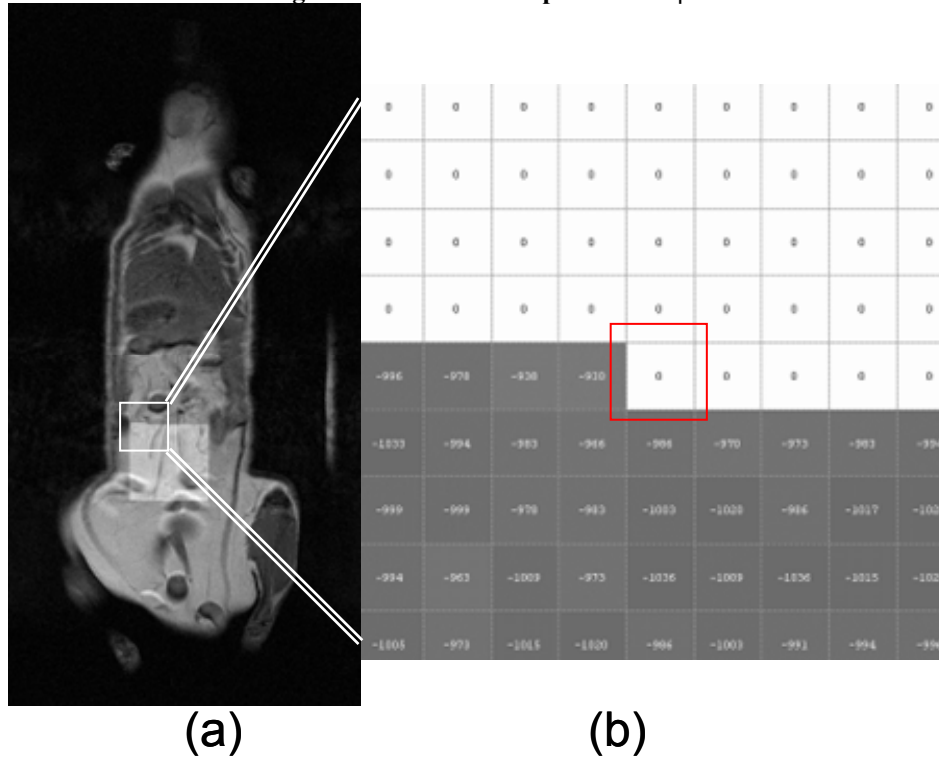
The planar extrapolation of ψ is shown for an intermediate step in the algorithm with an overlay on the magnitude image in (a). Given the neighborhood of solved ψ values in the lower half of the window, what is the correct choice for the current pixel in the red box (b)? The correct choice should make fat the dominant component because the window is currently centered over adipose tissue, but aliases of ψ still interfere with the choice.

In this specific example, the pixel at the center of the window has ψ_W=147 Hz, ψ_F=-904 Hz, 1/ΔTE = 3153.6 Hz, and the aliased solutions include (-4058 Hz, -3006 Hz) and (2250 Hz, 3301 Hz). The neighborhood surrounding the pixel has ψ values with a median of -998 Hz, min of -1089 Hz, max -837 Hz, mean -995 Hz, and weighted planar extrapolation of -989 Hz (slope along X: ψ_x=2.7 Hz/pixel, slope along Y: ψ_y=1.0 Hz/pixel, offset=-1010). The choice is easily and correctly picked as -904 Hz because it is the closest of the possible solutions (minimum absolute difference) to the planar extrapolation, but other regions are not as easy to solve. Instead of using planar extrapolation, other filters could be used. For example, the median of this neighborhood was fairly close to the correct solution, as was the mean. Computing the median of every

possible neighborhood during the extrapolation would be quite computationally expensive, but possibly very effective at rejecting outlier values. In contrast, computing the average of every neighborhood is relatively fast, but also very susceptible to outliers. A combination of planar extrapolation and averaging offers the best tradeoff between computational speed and being responsive to true changes in ψ.

Planar extrapolation technique is prone to propagating errors throughout the image if any part of the region growing trajectory produces incorrect results because the incorrectly solved pixels will be used on a later iteration for extrapolation. Therefore errors must be carefully avoided in every pixel.

We modify the planar extrapolation in several important ways. Firstly, the weighting is changed to be binary instead of using the original pixel intensities of the input images. This removes the effects of T1-weighting from the estimation, which is a problem in spin echo images with a short TR. Thus, fat pixels are given unusually high weight during the extrapolation, which can result in errors. All non-air pixels should be weighted equally. Secondly, the planar extrapolation should have maximum limits on the slopes of the x and y components. Error propagation frequently occurs when ψ_x or ψ_y is unrealistically large, which causes the wrong value of ψ to be chosen. This will cause later regions of the image to extrapolate to even larger values of ψ. Therefore, if ψ_x or ψ_y is above a set threshold then only the weighted average value of ψ_0 is used to predict the correct solution. On a pixel-by-pixel basis this has the effect of switching from planar extrapolation filter to 2D averaging filter, which is more robust but less responsive to changes in ψ.

3.2   *Methods and Materials*

High resolution shifted spin echo scans were acquired on a Bruker Biospec 7T/30cm of two 26 week old C57BL/6J male mice, one each on a high fat diet mice and a low fat diet (Jackson Laboratory Diet-Induced Obesity Service, D12492i 60 kcal% fat chow vs. D12450Bi, 10 kcal% fat chow, Research Diets, Inc.). A T1-weighted Rapid Acquisition with Relaxation Enhancement (RARE) sequence with varying echo asymmetry delays was used to achieve $\pi/6$, $5\pi/6$, and $3\pi/2$ radian shifts between fat and water (TR=1087 ms/gated, TE=9.1 ms, 102 x 40 to 102 x 50 mm FOV, 512x256 matrix, 4 averages, and echo asymmetry delays of 79, 396, and 714 us). Animal studies were conducted under a protocol approved by the Institutional Animal Care and Use Committee at Case Western Reserve University.

The method was implemented on a desktop computer with 32GB RAM, dual Intel Xeon X5450 3.0 GHz processors, an Nvidia Quadro FX5800 (4GB RAM, 240 cores, 400 MHz clock), and Matlab R2009a 64bit with Accelereyes Jacket v1.0.2. Jacket is a library that makes GPU computation easier to implement via calling Nvidia CUDA routines directly from Matlab.

Brent's method was compared to golden section search using a mouse dataset. Signals of one pixel at 3 TEs were extracted from the mouse dataset in a pixel inside the spinal muscles (i.e. near the center of the FOV and known to be dominantly water). An initial bracket was constructed using downhill search starting at $\psi=0$ (88), and then each method was run from this initial condition. One function evaluation was allowed per iteration of the optimization routine. Iteration was stopped when the error in ψ was under 0.1 Hz.

The speed of the GPU implementation was compared to an equivalent CPU implementation. A 512x256x3 mouse image was reconstructed using Eqs. (3.2) and (3.3) with 1000 fixed values of ψ in each pixel to test the running speed of the GPU and CPU implementations. The image was downsampled along the Y direction logarithmically from 512 pixels to down to 5 pixels to change the size of the dataset and determine the minimum image size where the computational speed of the GPU outweighs the cost of transferring the data across the bus to the GPU. Additionally, a CPU-only test was performed by changing the number of concurrent threads allowed in Matlab and repeating the reconstructions to determine how much benefit could be derived from using the multiple CPU cores (up to eight on this system).

The robustness of the new planar extraction routine was compared with methods from the literature. The IDEAL reconstruction methods of Reeder et al. (46) and Yu et al. were implemented (48) in Matlab. Mouse images with difficult image features (i.e. quickly varying B0 inhomogeneity around the lungs and intestines, cardiac motion, and multiple ψ aliases across the full FOV) were chosen to test the different planar extrapolation routines. Each routine was initialized at the same point at the center of mass of the image. The unconstrained planar extrapolation routine by Yu et al. (48) was attempted with window sizes of 25x25, 30x30, and 20x20 pixels to test if empirically changing the window size would improve the planar extrapolation as suggested by the authors. The new method was tested with a 25x25 pixel window and limiting both slopes ψ_x and ψ_y to 15 Hz/pixel (i.e. 1.8 mT/m).

The proposed limited slope method was compared to the unconstrained planar extrapolation routine by Yu et al. (48) given the same initial conditions in a large study of

mouse images. An image operator analyzed a total of 236 images in 12 mouse datasets using both algorithms. The operator determined the ground truth fat and water assignments using a manual correction algorithm, as follows. Initially, all pixels were assigned to the ψ_W solution (i.e. where water is assigned as the dominant species in each voxel). The operator repeatedly used a 20x20 median filter on the ψ map until the incorrectly assigned pixels in the adipose tissue were reassigned to the correct solution, as per the manual correction of Reeder et al. (46). The operator compared the ground truth fat and water estimates to those of starting each extrapolation method at the same pixel coordinates on the initial ψ_W solution. The number of incorrectly assigned pixels was found by thresholding a 75% change in signal intensity of the normalized absolute the water estimate as compared to the ground truth water estimate. Air pixels were excluded from this computation by applying a threshold to the original magnitude image of $\mu_{air}+3*\sigma_{air}$, where the mean (μ_{air}) and standard deviation (σ_{air}) of air intensity was automatically determined from the 10x10 pixels in the upper right hand corner of the image.

3.3   Results

Golden section search required more function evaluation than Brent's method to achieve the same error tolerance in ψ (13 vs. 7 function evaluations in the example pixel, Figure 3-3). Over the non-air pixels in the mouse image shown in Figure 3-5, the median of the difference in the number of function evaluations of golden section search minus the number of function evaluations of Brent's method was three (min -4, max 8). The total number of iterations depended on the configuration of the brackets from the initial bracketing routine, but which was not counted against either optimization method. Brent's

method converged quickly when the parabolic fit to the initial bracket was good. In a very limited number of pixels (1.0% of all non-air pixels), Brent's method actually required more iterations due to inefficient switching between the parabolic and golden steps. The vast majority of pixels (93.9%) converged more quickly with Brent's method.

Figure 3-3. Brent's Method Applied to IDEAL Estimation
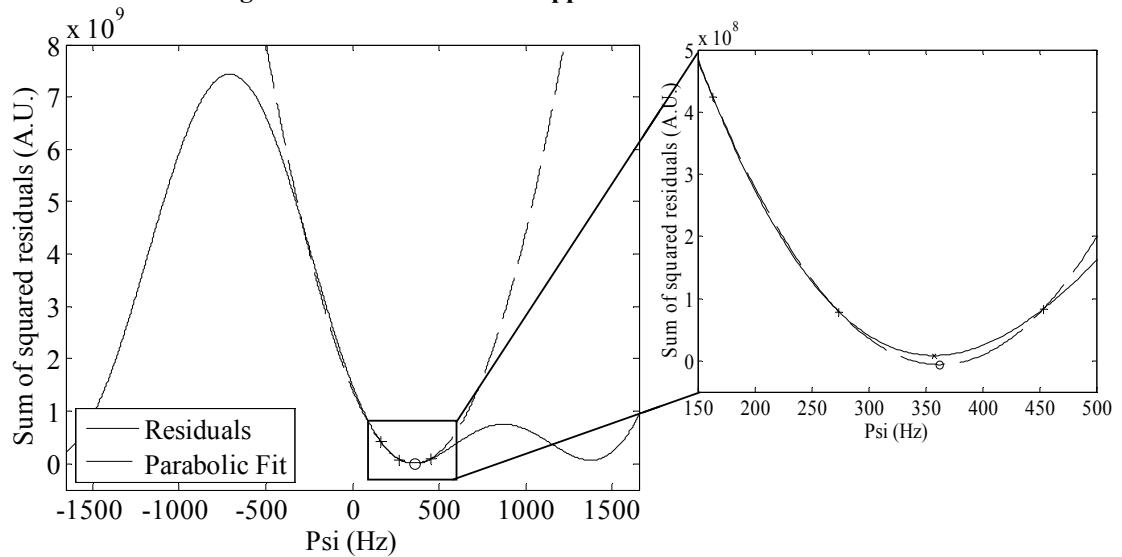
Brent's method uses inverse quadratic interpolation to quickly find minima in the residuals vs. Ψ curve. The initial brackets (crosses, +) are used to fit a parabola and "jump" to the apex, which is near the minimum (circle and x, small inset graph). For the same initial conditions in this example, Brent's method isolates the minimum in 7 iterations as compared to 13 iterations for golden section search.

Brent's method required fewer iterations to isolate minima in ψ than golden section search (7 vs. 13 iterations, respectively, for the example in Figure 3-3). Over the non-air pixels in a 512x256 test image (shown in Figure 3-7), Brent's method required fewer iterations than golden section search in over 93% of non-air pixels (6.8 ± 1.5 vs. 9.6 ± 1.6 iterations, $P<0.01$, Wilcoxon signed rank test, Figure 3-4). The center of the histograms of the number of iterations showed a reduction of 3 iterations for most pixels.

Figure 3-4. Histograms of Iterations.
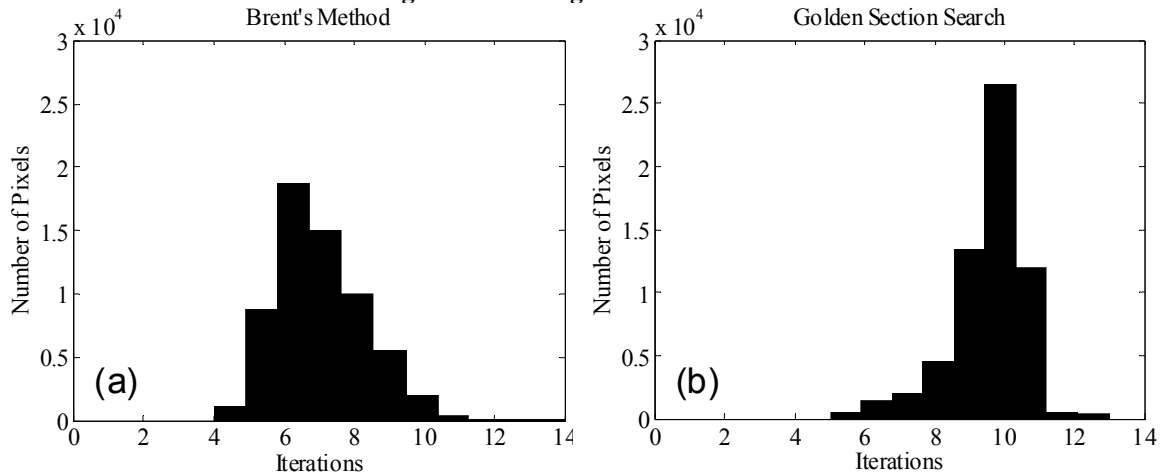
Histograms of the number of iterations to solve the non-air pixels in a 512x256 test image (displayed in Fig 2) demonstrate that Brent's method typically requires fewer iterations. Starting from the same initial conditions, the iterations required for each method to isolate the minima were recorded. Brent's method required fewer iterations than golden section search in over 93% of non-air pixels (6.8 ± 1.5 vs. 9.6 ± 1.6 iterations, $P<0.01$ Wilcoxon signed rank test).

The GPU implementation was ~50% faster than the CPU-only implementation in the full sized 512x256x3 image (23.5 s vs. 44.7 s, Figure 3-5-a). The CPU implementation became faster only for much smaller images, 24x256x3 or smaller (i.e. 6000 or fewer pixels). The shapes of the curves suggest that the speed advantage of the GPU will continue to improve over the CPU for images larger than 512x256x3. The CPU-only test with multithreading showed that images all sizes were faster using more threads, but there were significant diminishing returns (Figure 3-5-b). Utilizing up to 4 cores (i.e. 4 threads) improved reconstruction speed relative to not multithreading (70.0 s vs. 48.0 s for the 512x256x3 image), but using the maximum 8 threads provided <8% additional speedup relative to 4 threads (e.g. 44.6 s vs. 48.0 s). CPU mulithreading did not significantly affect reconstruction speed when the GPU was used (<5%, i.e. 0.9 s or less, data not shown).

Figure 3-5. CPU vs. GPU Reconstruction Time
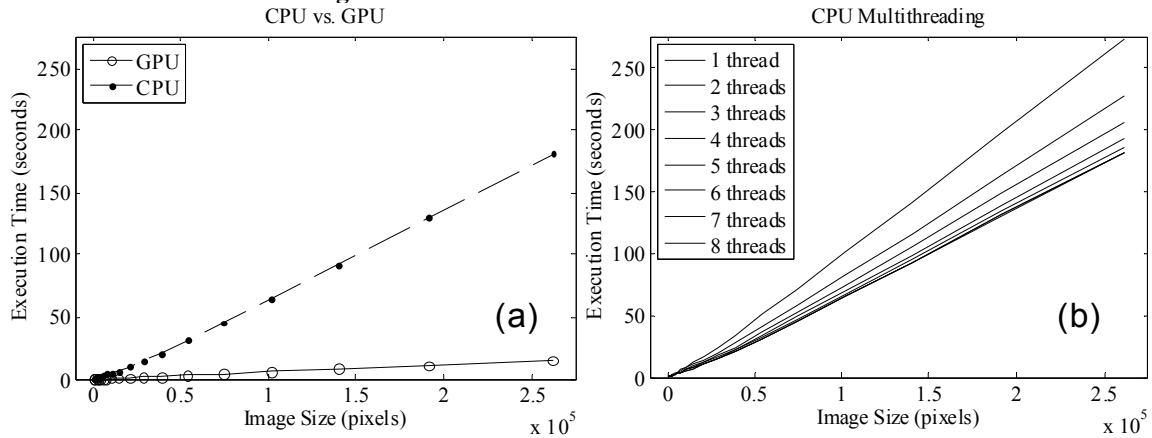
GPU versus CPU processing time for IDEAL reconstruction. (a) GPU and CPU execution times are plotted as a function of image size for a 3 TE reconstruction (N=11 repetitions of the reconstruction, dropping the first and averaging the others). For images of all sizes, the GPU was faster than the CPU (P<0.01), and for a 512x256 image, execution time was ~10X faster on the GPU as compared to the CPU with 8 threads (8.6±0.2 vs. 92.0±0.3 s, mean ± 1 s.d., P<0.01). (b) Execution time is plotted as a function of number of threads on an 8 core system. CPU-only performance improved from 1 to 4 threads, but improved relatively little with more threads. For the 512x256 image, 4 threads were 43% faster than 1 thread (98.7±0.3 vs. 141.1±0.4 s, P<0.01) but 8 threads were only 7% faster than 4 threads (92.0±0.3 vs. 98.7±0.3 s, P<0.01).

The GPU implementation was faster than the CPU for images of all sizes, and the advantage of the GPU improved with larger image sizes (Figure 3-6). Whereas the ratio of the CPU to GPU execution times was only 2.6 for the at the smallest image size tested (512 pixels), the ratio increased to 11.6 for the largest image size tested (261,888 pixels). The trajectory of the curves suggests that the speed advantage of the GPU will continue to improve over the CPU for larger images.

Figure 3-6. CPU/GPU Execution Time Ratio

GPU Speedup Relative to CPU
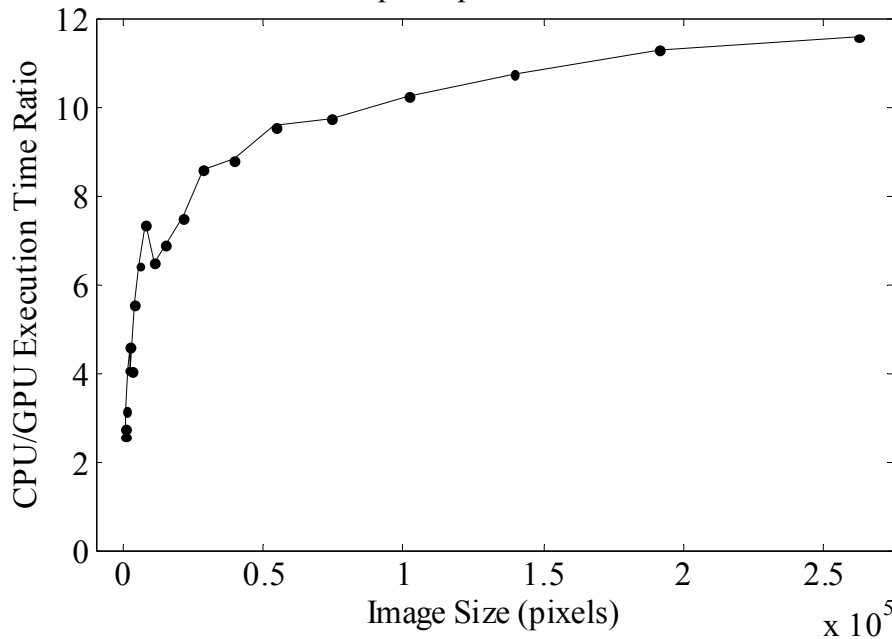
The speedup provided by the GPU increases as a function of the image size. The ratio of the CPU to GPU execution times was only 2.6 at the smallest image size tested (512 pixels) but the ratio increased to 11.6 for the largest image size tested (512x512 pixels). The ratio does not appear to increase further for larger images. Considering a very high resolution image of 2048x2048 (4.2 million pixels) with 3 TEs, the trend extrapolates to an execution time on 47.8 min on the CPU as compared to only 4.1 min on the GPU.

Planar extrapolation was much more successful when the *a priori* limits were applied to the linear slopes (Figure 3-7). The unsolved ψ image (Figure 3-7-b) contained ψ aliases of +3150 Hz and -3150 Hz near the top and bottom of the image (head and tail, respectively). Planar extrapolation failed in these regions and caused errors of over 3150 Hz to propagate past the lungs and intestines even when different window sizes were used (Figure 3-7-c, d, and e). The new algorithm was able to successfully solve this image (Figure 3-7-f), which was typical among other image slices in this algorithm. Multiple seed points were attempted to fix the method of Yu et al. (48), but all of them failed with similar propagated errors. In contrast, the limited slope algorithm was much less sensitive to the choice of the seed point.

Figure 3-7. Comparison of Planar Extrapolation Techniques

<div align="center">

(a)   (b)   (c)   (d)   (e)   (f)

</div>
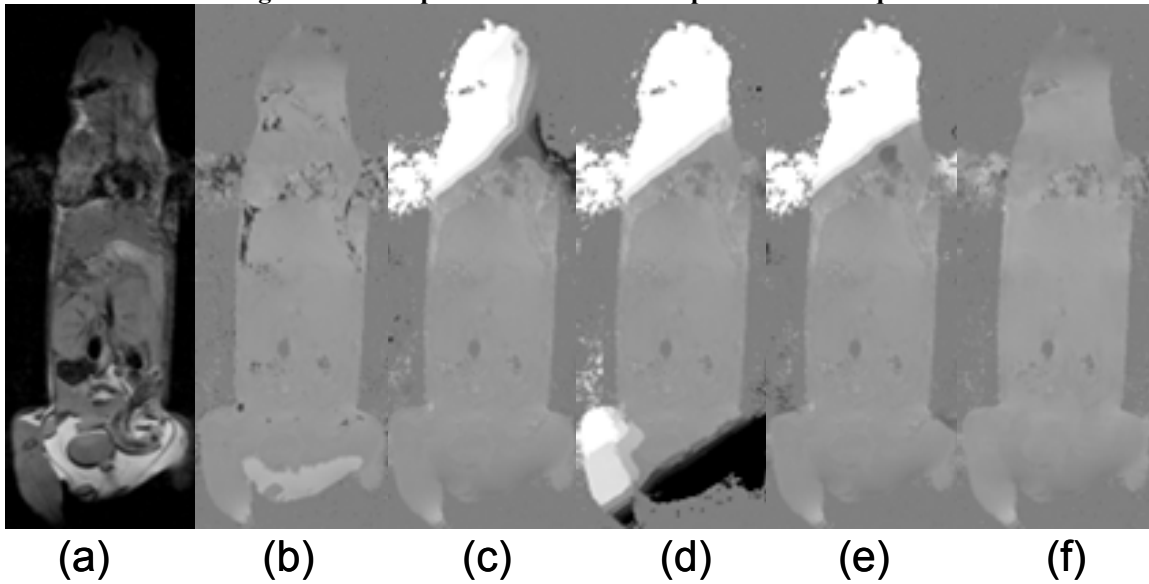
Comparison of the planar extrapolation (PE) and the modified planar extrapolation (MPE) algorithms. The reference magnitude image (a) and initial ψ map with many errors (b) are shown. When PE is performed with a variety of window sizes, 20x20, 25x25, and 30x30 (c-e, respectively), errors result when the window passes through the lungs and/or intestines. In comparison, MPE with a 25x25 window (f) does not suffer from these artifacts and finds a high quality ψ map. Those few remaining irregularities in ψ tend to occur in the lungs or the heart where fat-water calculations are corrupted by motion.

The other IDEAL reconstruction algorithms tested failed on the example dataset (Figure 3-8). The IDEAL reconstruction method of Reeder et al. (46) failed in two parts of the images where initializing the reconstruction at $\psi=0$ did not converge to the correct solution for fat and water. The method of Yu et al. (48) assumes that the center of mass of the image converges to the correct solution when initialized to $\psi=0$, which is false in this dataset. In contrast, the proposed method was able to correctly separate fat and water throughout the image.

Figure 3-8. Comparison of IDEAL reconstructions
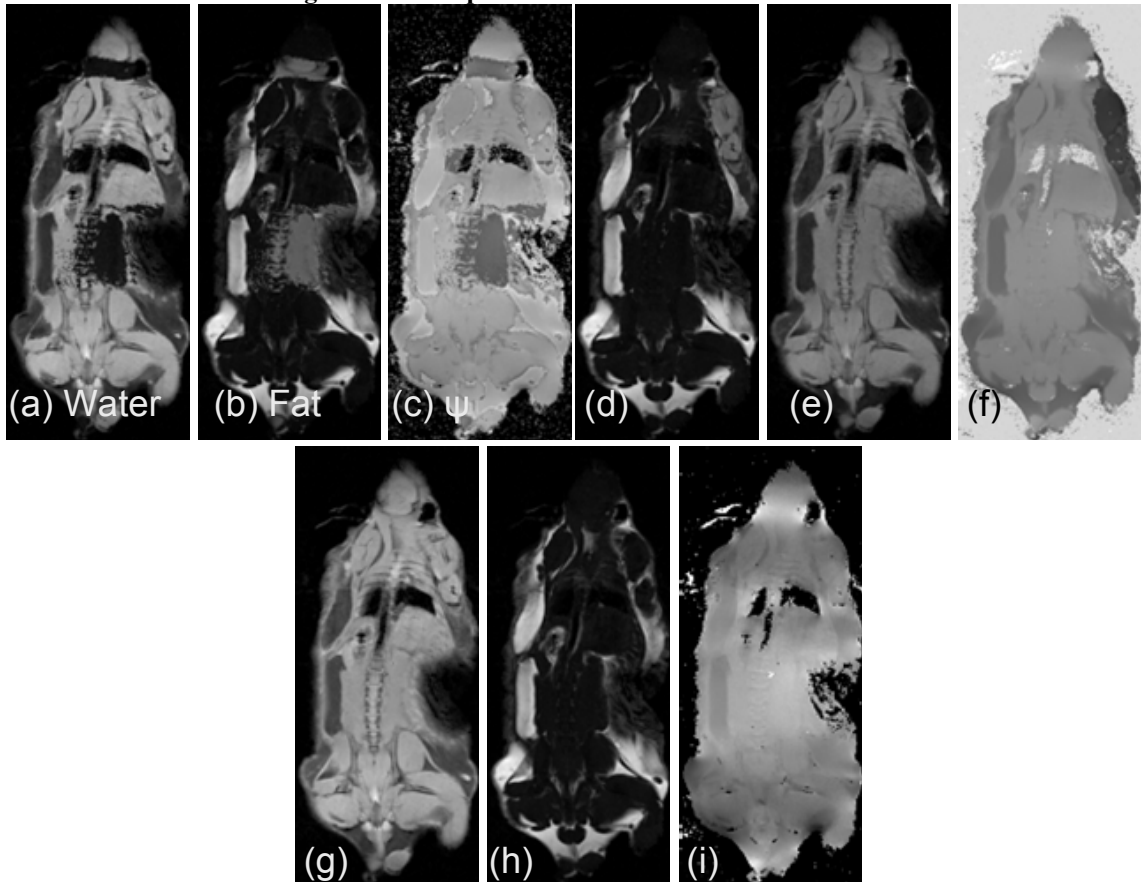
Comparison of IDEAL algorithms shows the advantages of the new technique. The original IDEAL algorithm (a-c) incorrectly estimates fat as water and vice versa in the head, liver, and mid-spine. The region growing IDEAL algorithm (d-f) assumes the center of mass is a reliable starting point, which is false in this dataset, and therefore errors are propagated across the image. The proposed method (g-i) is able to correctly separate fat and water.

The limited slope extrapolation performed significantly better ($P<10^{-4}$) than the standard extrapolation routine of Yu et al., as determined a Wilcoxon-rank-sum test of the number of incorrectly assigned pixels in a study of 236 images in 12 mouse datasets (Figure 3-9). The error rate of the proposed method was six times lower than the standard extrapolation routine (0.7% vs. 4.5% of incorrectly assigned pixels normalized to the total number of non-air pixels). Most errors in the proposed method were due to either disconnected regions or respiratory artifacts.

Figure 3-9. Comparison of Errors
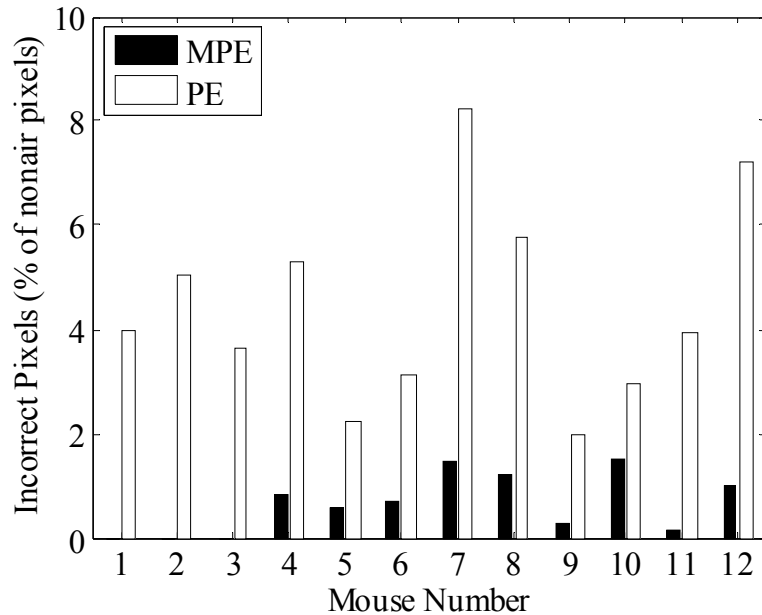
Comparison of number of pixels erroneously assigned (fat as water or vice versa) among a study of six low fat diet mice (mice 1-6) and high fat diet mice (7-12). A total of 236 images were processed by both algorithms and results were compared to the same images processed with careful manual editing. Air pixels were excluded by applying a threshold to the magnitude image. The number of pixels incorrectly assigned by MPE is significantly lower than PE (P < 10-4).

3.4   Discussion

A robust IDEAL reconstruction was developed for reconstructing mouse images on a high field scanner, and a commodity graphics card was used to speed up the computations. The vectorized mathematical equations were used to enable IDEAL to take advantage of the massively parallel graphics card and the multithreading of a multi-core CPU. Brent's method was used to quickly "jump" to the correct solution for ψ when minimizing the residuals, which reduced the number of iterations needed to solve the image. The planar extrapolation model was improved by limiting the fitted slopes of the extrapolation and switching to an averaging filter in the case of a bad fit, which eliminated the propagation of errors throughout the image.

The speed advantages of using a GPU will become more important as the trend towards higher resolution images continues to produce larger MRI datasets. This work

demonstrates that 50% speedups are possible despite a significant disadvantage in clock speed (3.0 GHz CPU vs. 400 MHz GPU) and the need to transfer the entire image sets across the video bus. The implementation might be improved further by doing a pure GPU calculation, but our tests indicate that the CPU is actually faster for evaluating Brent's method due to the amount of branching logic.

Brent's method is only one of a number of possible improvements to the optimization. Implementing a vectorized version of Newton's method appears promising because analytical first and second derivatives with respect to ψ are available for Eq. (3.4). Newton's method typically has the fastest possible convergence among line search algorithms if the starting condition is close enough to the minimum though caveats remain about maintaining brackets and minimum step sizes. It remains to be seen if algebraic decomposition and harmonic retrieval (89) are faster than the new method because they involve much more computationally expensive mathematical operations (i.e. per-pixel singular value decomposition). However, algebraic decomposition cannot account for T2* decay, whereas the vectorized forms of Eqs. (3.2)-(3.4) can model T2* decay without modification. Future work will include an optimization routine that estimates the imaginary component of ψ (i.e. T2* decay).

In conclusion, a robust and efficient technique for reconstructing IDEAL fat and water images on a high field scanner was developed and implemented on a commodity graphics card, and a significant reduction in reconstruction time was achieved.

Chapter 4   IDEAL Mouse Imaging on a High Field Scanner

4.1   Background

The goal of this study was to develop a robust imaging technique for phenotyping the C57BL/6J mouse model of dietary obesity. On a high fat diet, the C57BL/6J mouse gains body weight and accumulates fat in adipose tissues and in the liver. We demonstrate the feasibility and effectiveness of applying IDEAL at 7T with relevant validation. Future work will allow for larger, longitudinal studies without the need for validating the phenotypes by euthanasia.

CHESS imaging is the gold standard due to ease of implementation. We have shown that CHESS imaging can be used to phenotype rats on a 1.5T clinical scanner (90). There is an opportunity to get high resolution images with better SNR by using a high field scanner designed specifically for small animals. However, high field scanners have a non-uniform main magnetic field, which must be corrected to estimate fat and water signals. We chose the IDEAL framework for this study and compared it to CHESS imaging. One possible alternative to IDEAL is the 3-point Dixon method to compensate for field inhomogeneity, but the post processing phase unwrapping is unreliable.

CHESS imaging fails or inadequately separates fat and water in the presence of large field inhomogeneity, which hinders quantification. CHESS imaging can fail on a single animal due to incorrectly setting the center frequency to fat, which can be a problem in obese rodents. It can also introduce inconsistencies in a study of many

animals where the product automated shimming does not work well every time. Our hypothesis is that IDEAL imaging is more robust than CHESS imaging at 7T.

This work is the first to report an obese mouse imaging study using IDEAL at 7T. We also introduce a simple but effective T1 and T2 correction in post-processing instead of acquiring extra images.

4.1.1 Theory

IDEAL primarily uses phase information to separate fat and water. We assume that the effects of T2* decay can be ignored because the imaging acquisition uses extremely short echo shifts (e.g. 700 us or less). The IDEAL estimates will be biased by the T1 and T2 contrast inherent in the input images, which we model as follows.

$$\rho_{f,w} = M_{f,w} e^{-TE/T2_{f,w}} \left(1 - e^{-TR/T1_{f,w}}\right) \tag{4.1}$$

The IDEAL estimates (ρ_f and ρ_w) are biased by the T1 and T2 effects ($T1_f$, $T1_w$, $T2_f$, and $T2_w$). We want to measure the proton density (M_f and M_w). We assume that T1 and T2 were measured or known *a priori*. The corrected fat and water estimates can be found by simple division.

$$M_{f,w} = \rho_{f,w} \bigg/ e^{-TE/T2_{f,w}} \left(1 - e^{-TR/T1_{f,w}}\right) \tag{4.2}$$

We correct all of these biases. The T1 of water will dominate the bias in Eq. (4.1) because gated, *in vivo* mouse imaging at 7T will require a TR on the order of 1 second, whereas *T1w* is much longer. We used the follow parameters for the phantom studies (T1W=2500 ms, T1F=850, T2W=25, T2F=70) and for mouse studies (T1W=2900 ms, T1F=500, T2W=360, T2F=32), based on measured T1 and T2 values (see Tables 1-3 and Methods).

CHESS imaging at 7T. As developed by Johnson et al. at 1.5T (90), CHESS imaging can be used to quantitatively estimate fat fractions. Different values must be substituted for the T1 and T2 corrections at 7T, but the ratio image still takes the following form.

$$I_r(x,y) = \frac{\rho_{0,F}(x,y)}{\rho_{0,F}(x,y) + \rho_{0,W}(x,y)} = \frac{\dfrac{I_F(x,y)}{[(1-e^{-TR/T1F})e^{-TE/T2F}]}}{\dfrac{I_F(x,y)}{[(1-e^{-TR/T1F})e^{-TE/T2F}]} + \dfrac{I_{FW}(x,y) - I_F(x,y)}{(1-e^{-TR/T1W})e^{-TE/T2W}}} \tag{4.3}$$

I_r is the ratio image after T1 and T2 corrections for both fat and water, and the other symbols have the same meanings as in Eq (4.1).

4.2 *Methods and Materials*

Animal studies. High resolution shifted spin echo scans were acquired of six high fat diet mice and six low fat diet mice (26 week old C57BL/6J males, Jackson Laboratory Diet-Induced Obesity Service, D12492i 60 kcal% fat chow vs. D12450Bi, 10 kcal% fat chow, Research Diets, Inc.). A T1-weighted Rapid Acquisition with Relaxation Enhancement (RARE) sequence with varying echo asymmetry delays was used to achieve $\pi/6$, $5\pi/6$, and $3\pi/2$ radian shifts between fat and water (TR=1087 ms/gated, TE=9.1 ms, 102 x 40 to 102 x 50 mm FOV, 512x256 matrix, 4 averages, and echo asymmetry delays of 79, 396, and 714 us). For comparison to CHESS imaging, two additional in-phase scans were acquired with and without CHESS water saturation. T1 was measured in one high fat diet animal and one low fat diet animal using a spin echo scan repeated with 8 different TRs (TE=12.6 ms, TR=690, 811, 955, 1128, 1351, 1661, 2174, and 4000 ms, identical geometry to *in vivo* IDEAL scans). T2 was measured in the

same two mice using a multiecho spin echo scan (16 TE's equally spaced from 9.7 to 155 ms, TR=4000 ms).

Mice were weighed and euthanized immediately after imaging, and the right caudate lobe of the liver was dissected and snap-frozen in liquid nitrogen for triglyceride analysis via chemical lipid extraction. The concentration of triglycerides was measured by the optical density of glycerol backbones at 900 nm and converted into absolute concentration via a set of known concentration glycerol phantoms. The right median lobe was snap-frozen for histological analysis using Hematoxylin and Eosin (H&E) and Oil-Red-O (ORO) stains.

Phantom validation studies. Fat-water phantoms were imaged using the above protocol maintaining all parameters except acquiring only a single slice and disabling respiratory gating. Intralipid (20% soybean oil by weight, Sigma Aldrich) was diluted with deionized water (Millipore MilliQ deionizing water system) to create 50 ml conical tubes of 20%, 15%, 10%, and 5% soybean oil by weight. As a reference, two additional tubes of unmixed, pure soybean oil and deionized water were also imaged (herein referred to as 100% and 0% soybean oil by weight). Additional images were acquired with a very long TR (15 seconds) as a reference for comparison with the post-processing T1 correction. MR spectra were acquired in each tube individually using PRESS to model the in vivo imaging parameters (TR=1087 ms, TE=9.1 ms, 8 x 8 x 8 mm^3 voxel, 30 averages).

Semi-automatic IDEAL Reconstruction. An interactive IDEAL reconstruction program was implemented in Matlab (The Mathworks Inc., Novi, MI). As described by Lu et al. (51), both minima in each pixel were found. The minimum corresponding to

having water as the dominant component was then assigned in each pixel. This will be the correct Ψ value for all water-dominated tissues, and it will be incorrect in all fat-dominated tissues (e.g. adipose tissue). But the adipose tissues are irregular in shape, and they are often surrounded by water-dominated tissues. Using this observation, we use a 2D median filter to fix the incorrectly labeled adipose tissue regions. The current Ψ value in every pixel in the image is compared to the median of a moving 2D median filter of 15x15 pixels (size empirically chosen based on 200um x 200um in-plane resolution). If the difference between the Ψ value and the median of the neighborhood is over half of the fat-water frequency aliasing factor (525 Hz at 7T) then the pixel is "flipped" to the alternative solution (i.e. the water estimate is switched for the fat estimate, and vice versa, and the corresponding Ψ values are also flipped). This process is repeated by the operator until no further visual changes occur. We found this process to be adequate for the majority of images, which were typically corrected in about 10 sec.

Semi-automatic Image Segmentation. We used the image analysis methods of Johnson et al. (90). Abdominal cavity volumes were manually traced in Amira (Mercury Computer Systems, Berlin, Germany) and imported into Matlab, along with the output of the interactive IDEAL reconstruction program. In brief, a lower bound threshold was automatically calculated and applied to the magnitude of the in-phase image to remove air by thresholding. The T1- and T2-corrected ratio of the two additional in-phase scans acquired with and without CHESS water saturation was used to segment adipose tissues from non-adipose tissues using a constant threshold of 0.50. Visceral and subcutaneous adipose tissue volumes were calculated as the size of one voxel times the number of segmented adipose tissue voxels inside and outside the abdominal cavity, respectively.

All other non-air voxels were measured as non-adipose tissue. IDEAL analysis was performed in exactly the same way, except that the air threshold was applied to the magnitude of the π/6 image, and the per-pixel fat ratio was calculated using the magnitudes of the final IDEAL fat and water estimates. Volumes of visceral and subcutaneous adipose tissue and non-adipose were calculated as described before for the CHESS analysis again using a constant threshold of 0.50.

Signal Intensity Comparisons. An operator manually traced ROI's of 30-50 pixels in the ratio images generated by both CHESS imaging and IDEAL in Amira. ROI's were placed in the right caudate lobe of the liver, the lower right hindlimb muscles, the visceral adipose tissue, and the kidneys. The pixel values were tested for statistically significant differences between the diets using an unpaired students t test. Fat-water contrast to noise ratio (CNR) was calculated by computing the mean and standard deviation of pixels in two 10x10 ROIs in kidneys (e.g. water, A) and adipose tissue (e.g. fat, B) as per Eq (4.4).

$$\text{CNR}(A,B) = \frac{|\text{Mean}(A) - \text{Mean}(B)|}{\sqrt{\text{Standard Dev}(A)^2 / 2 + \text{Standard Dev}(B)^2 / 2}} \tag{4.4}$$

4.3   Results

4.3.1   Phantom validation study

IDEAL fat fraction estimates in the oil-water phantoms demonstrated the feasibility of measuring small changes in low fat fractions (<20% oil by weight). IDEAL fat fraction maps were found to be visually correlated with the known weight fraction of the emulsions (Figure 4-1-a). Nonlinearity and an unexpectedly high intercept (0.12) and

slope (0.76) were observed in the linear fit of uncorrected ratio (R^2=0.93, Figure 4-1-b). The T1 and T2 correction reduced the nonlinearity and intercept (0.04) and slope (0.70) and improved the linear fit (R^2=0.99, Figure 4-1-b).

Figure 4-1. Oil-Water Phantom at 7T
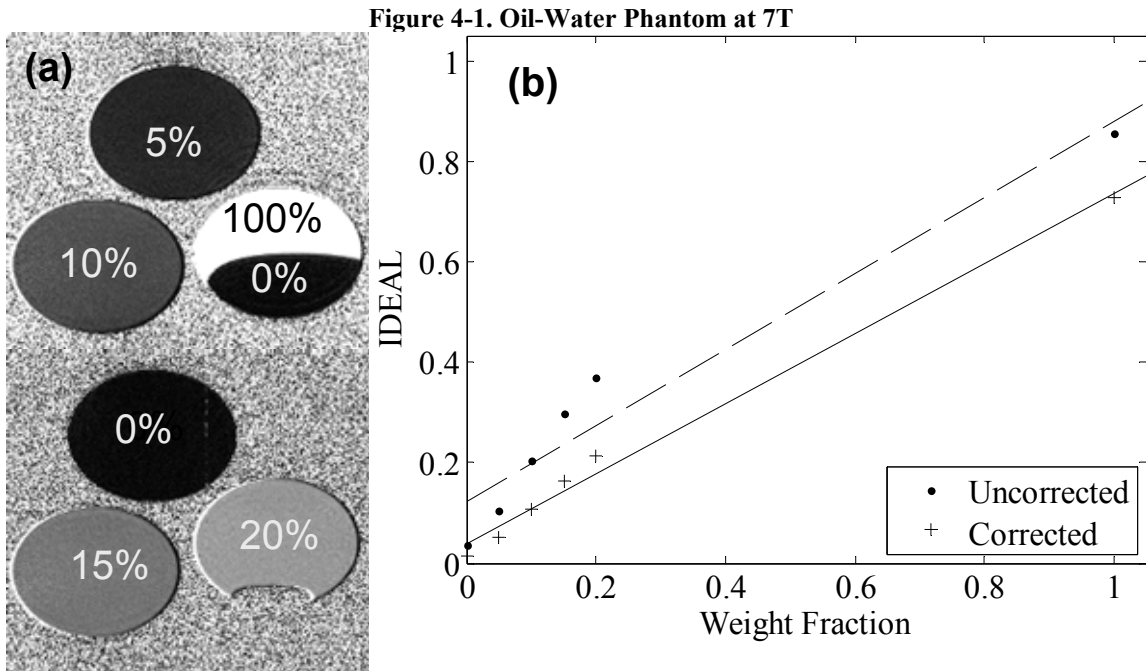
Oil-water phantom data demonstrate linearity of IDEAL fat fraction after T1 and T2 correction. a: Calculated fat fraction maps after T1 and T2 correction. b: Uncorrected IDEAL ratio vs. known oil concentration shows nonlinearity (R2=0.93). After correction, the IDEAL ratio is more linear (R2=0.99).

Agreement of the IDEAL measurements with MR spectroscopy was tested using a Bland-Altman plot (Figure 4-2). The in vivo imaging limitation of a short TR (1087 ms) caused 5% to 15% disagreement between the uncorrected ratio (Figure 4-2, closed circles) and MRS. The T1 and T2 corrections (Figure 4-2, diagonal X's) reduced this disagreement to 2% or less for all low concentrations but increased the disagreement for the pure oil phantom. The effects of just the T2 correction were investigated by repeating the experiment with a very long TR (15000 ms). Disagreement between the long TR IDEAL fractions and MRS was reduced from ~5% to 2% or less for all low concentrations (Figure 4-2, horizontal crosses vs. open circles).

**Figure 4-2. Bland-Altman Plot of Phantom Fat Fraction**
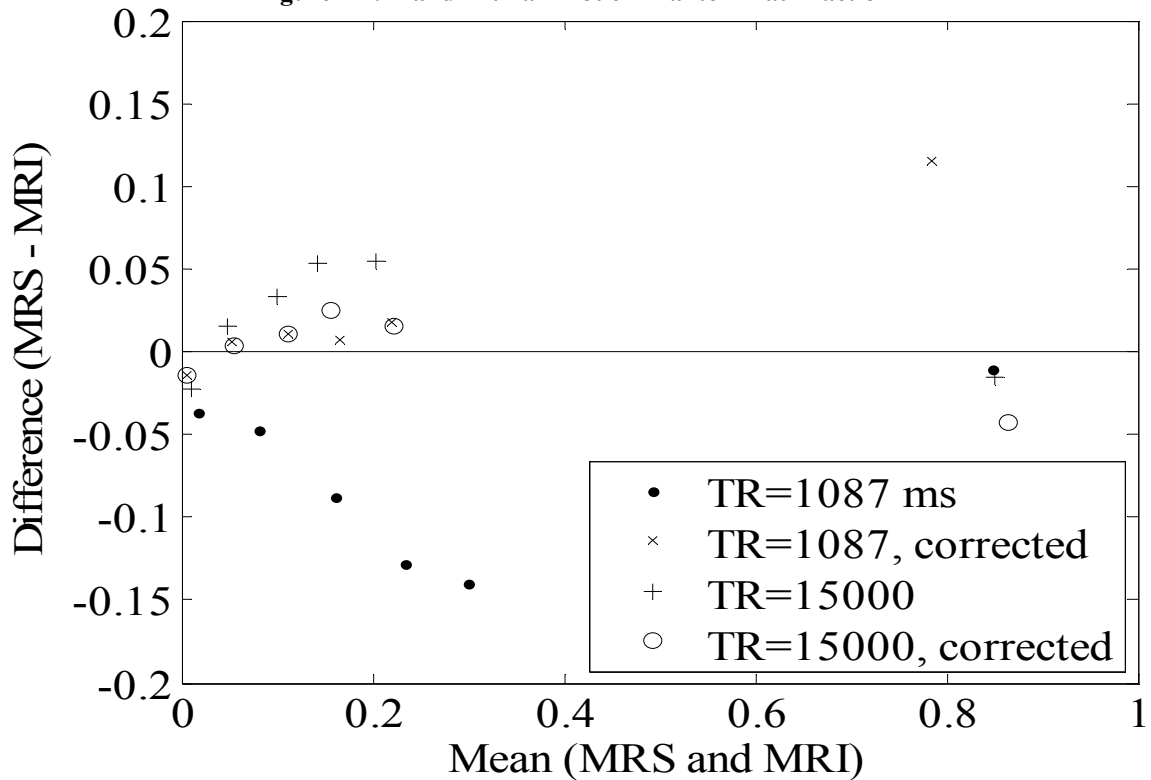
Bland-Altman plots of the oil-water phantom data demonstrate better agreement of IDEAL estimates with MRS after T1 and T2 corrections. Even at a very long TR, the correction improves the agreement of MRI and MRS.

4.3.2 Animal studies

The IDEAL ratio imaging technique produced robust tissue volume measurements *in vivo* despite receiver coil sensitivity inhomogeneity and field inhomogeneity (Figure 4-3). Signal intensity was not spatially uniform in the input T1-W images (e.g. compare top to bottom of Figure 4-3-a). Fat-water contrast was improved in the IDEAL water and fat estimates (CNR=19.5 in input images vs. 40.0 in IDEAL fat estimate images). The estimated field inhomogeneity map showed a wide range of offset from 300 Hz to 2000 Hz even in single slices (ψ map, Figure 4-3-d). The field inhomogeneity map also contained blurring and ringing artifacts, which were possibly a result of the RARE acquisition. The final T1 and T2 corrected ratio image was spatially uniform (Figure 4-3-e). Label images were created from the semi-automatic ratio image

analysis program to delineate the visceral adipose tissue (dark gray, Figure 4-3-f), non-visceral adipose tissue (white), air (black), and other muscles and organs (light gray).

Figure 4-3. IDEAL Mouse Images at 7T
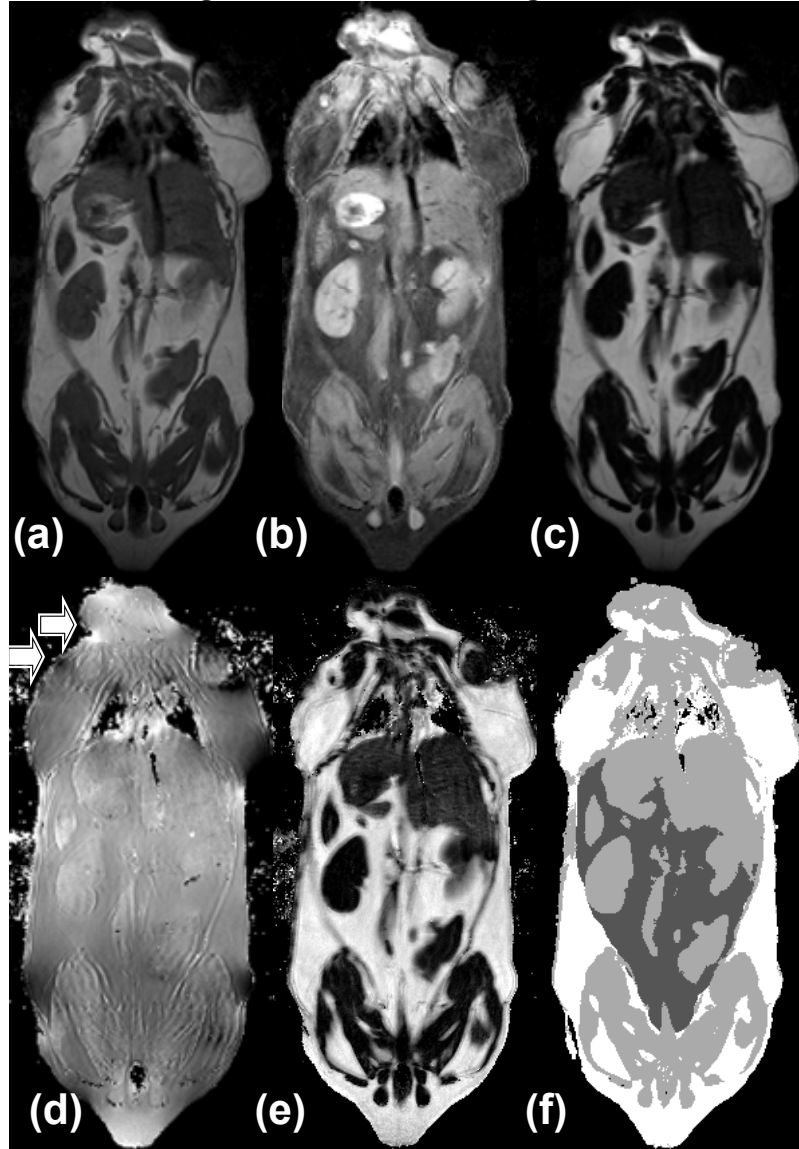
IDEAL image processing shows the challenges of 7T whole mouse imaging. T1-W input image (a) has significant receiver coil sensitivity inhomogeneity (e.g. top vs. bottom of image). The water (b) and fat (c) estimates retain this sensitivity inhomogeneity but provide improved fat-water contrast and tissue contrast (e.g. kidneys, liver, and muscles vs. adipose tissue depots). The corresponding ψ map (d) shows significant field inhomogeneity ranging from 300 Hz to 2000 Hz in this slice alone, sometimes over a small distance (arrows). The ratio image (e) removes the sensitivity inhomogeneity and enables semi-automatic quantification. The final label image (f) shows the segmentation of tissues tissues (non-visc. adipose tissue white, visc. dark gray, muscles and organs – gray, air – black).

IDEAL ratio images had consistent signal intensities in all slices of every mouse (Figure 4-4). Adipose tissue was reliably 82%±3%, and muscles were 4%±3%. Small

amounts of blurring and ringing due to the RARE acquisition were observed in many slices (e.g. Figure 4-4-a, b, c). Respiratory artifacts caused additional blurring in a limited number of slices (e.g. Figure 4-4-d).

Figure 4-4. Multiple Contiguous IDEAL Ratio Images
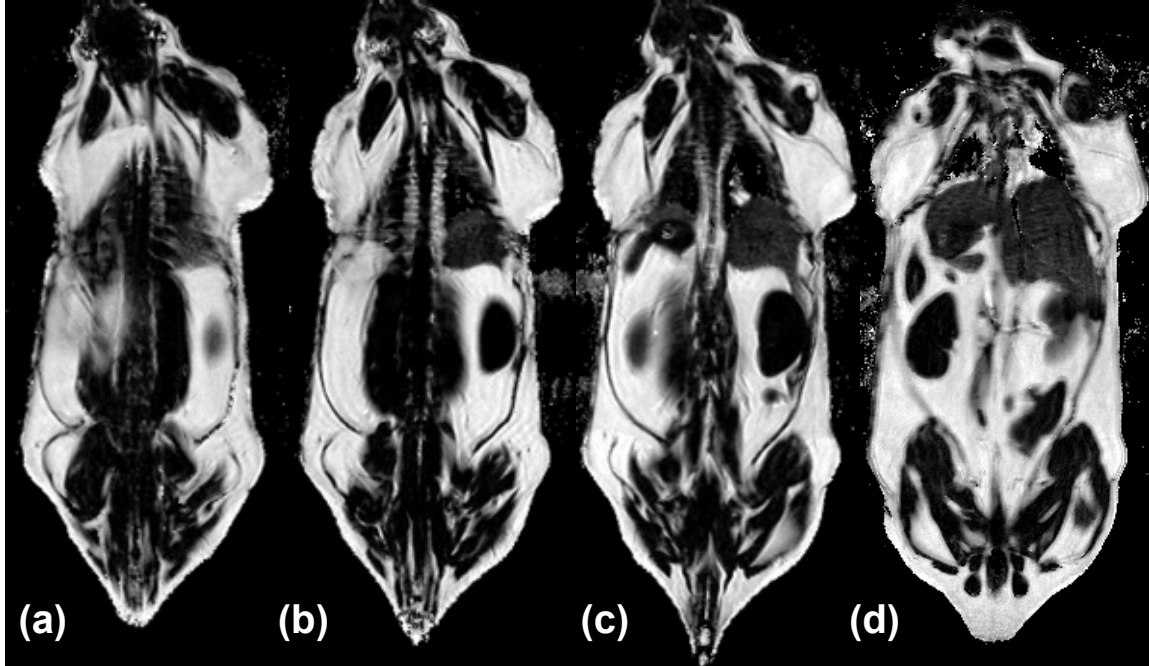
Multiple consecutive slices (a)-(d) are robustly estimated using the IDEAL ratio technique despite strong field inhomogeneity.

Liver signal intensities in the corrected IDEAL ratio images were much higher in the high fat diet animals as compared to low fat diet animals (Figure 4-5-a and b, representative images). The intensities were uniformly low in the low fat diet animals (e.g. 3.1%±1.7%, Figure 4-5-a). A wider range of ratio intensities were observed among the high fat diet animals, corresponding to the degree of fat accumulation (e.g. 27.2%±5.4%, Figure 4-5-b). These differences were validated ex vivo by chemical lipid extraction (220.6 vs. 13.4 mg triglyceride per g liver in these two mice).

Figure 4-5. Livers of High and Low Fat Diet Mice
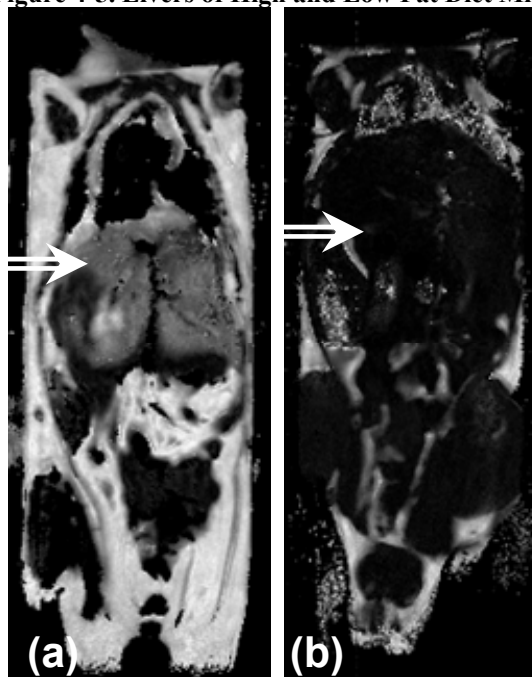
IDEAL ratio images of a high fat diet mouse (a) and a low fat diet mouse (b) show a huge difference in liver fat content (27.2%±5.4% vs. 3.1%±1.7%). This difference was validated by chemical lipid extraction (220.6 vs. 13.4 mg triglyceride per g liver).

IDEAL ratio signal intensities in the right caudate liver appeared to correlate linearly with the chemical lipid extraction assay (Figure 4-6). All of the low fat diet mice had very low intensities around 5% (corresponding to 20 mg/g TG/liver or less), whereas the high fat diet mice spanned a wide range from 12.5% to 31.0% (corresponding to 60 to 250 mg/g TG/liver). A linear fit of the IDEAL vs. chemical lipid extraction yielded an intercept of 0.03 and a slope of 0.0013 with a strong R^2 value of 0.90. High fat diet mice had significantly higher concentrations of liver lipids than the low fat diet mice whether measured by IDEAL (P=0.002) or by the chemical assay (P<0.001).

**Figure 4-6. IDEAL Liver Fat Fraction vs. Chemical Lipid Extraction**
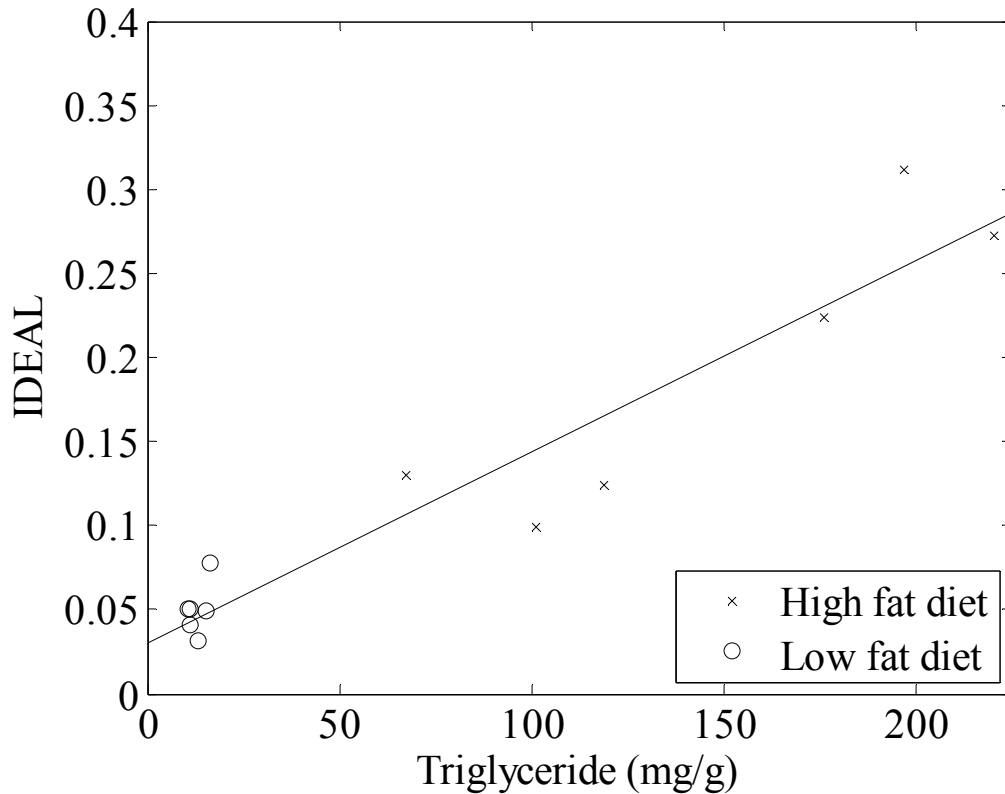
Liver triglycerides, as measured by a chemical assay, vary linearly with IDEAL ratio (R2=0.90). High fat diet mice had significantly higher concentrations of liver lipids, whether measured by IDEAL (P=0.002) or by the chemical assay (P<0.001).

Histological assessment of the mouse livers indicated significant intracellular lipid accumulations in the high fat diet animal (Figure 4-7-a and c, representative images) as compared to the low fat diet animal (Figure 4-7-b and d, also representative). Both the H&E and ORO stains were informative. Marked micro and macrovacuolation in hepatocytes was observed extending from the central vein mid-way to the portal triads in the high fat diet mouse (Figure 4-7-a, H&E). The large vacuoles stained positively using ORO stain, indicating the presence of intracellular lipid (Figure 4-7-c). In contrast, the low fat diet mouse had no significant cytoplasmic vacuolation (i.e. lipid vacuoles) on H&E (Figure 4-7-b) and no positive staining for cytoplasmic lipid on ORO (Figure 4-7-d). Histological assessments of the other mice were similar, though ORO staining

revealed a range of lipid staining among the high fat diet mice in agreement with the IDEAL ratio signal intensities and chemical lipid extraction assay.

Figure 4-7. Mouse Liver Histology
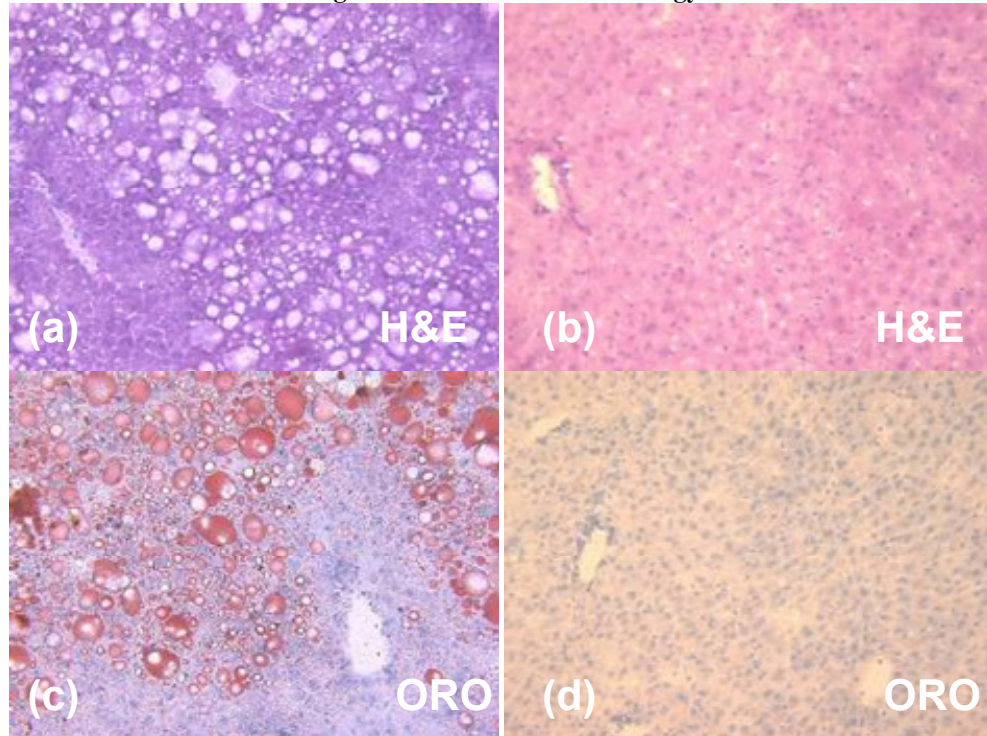
Histology of representative mouse livers shows significant intracellular lipid accumulations in the high fat diet animal (a and c) as compared to the low fat diet animal (b and d). Marked micro and macrovacuolation in hepatocytes extends from the central vein mid-way to the portal triads in the high fat diet mouse (a, H&E stain). In contrast, the low fat diet mouse had no significant cytoplasmic vacuolation (i.e. lipid vacuoles) on H&E (b) and no positive staining for cytoplasmic lipid on ORO (d).

Adipose tissue depots were significantly enlarged in the high fat diet mice as compared to the low fat diet mice when measured using IDEAL imaging (Figure 4-8). Visceral adipose tissue volumes were increased 9 fold in high vs. low fat diet mice, 6.4 ± 0.4 cm^3 vs. 0.7 ± 0.2 cm^3, respectively (P<0.001, Figure 4-8-a). Non-visceral adipose tissue volumes were increased 13 fold in high vs. low fat diet mice, 14.7 ± 2.0 cm^3 vs. 1.2 ± 0.3 cm^3, respectively (P<0.001, Figure 4-8-a).

Figure 4-8. Adipose Tissue Volumes in High and Low Fat Diet Mice
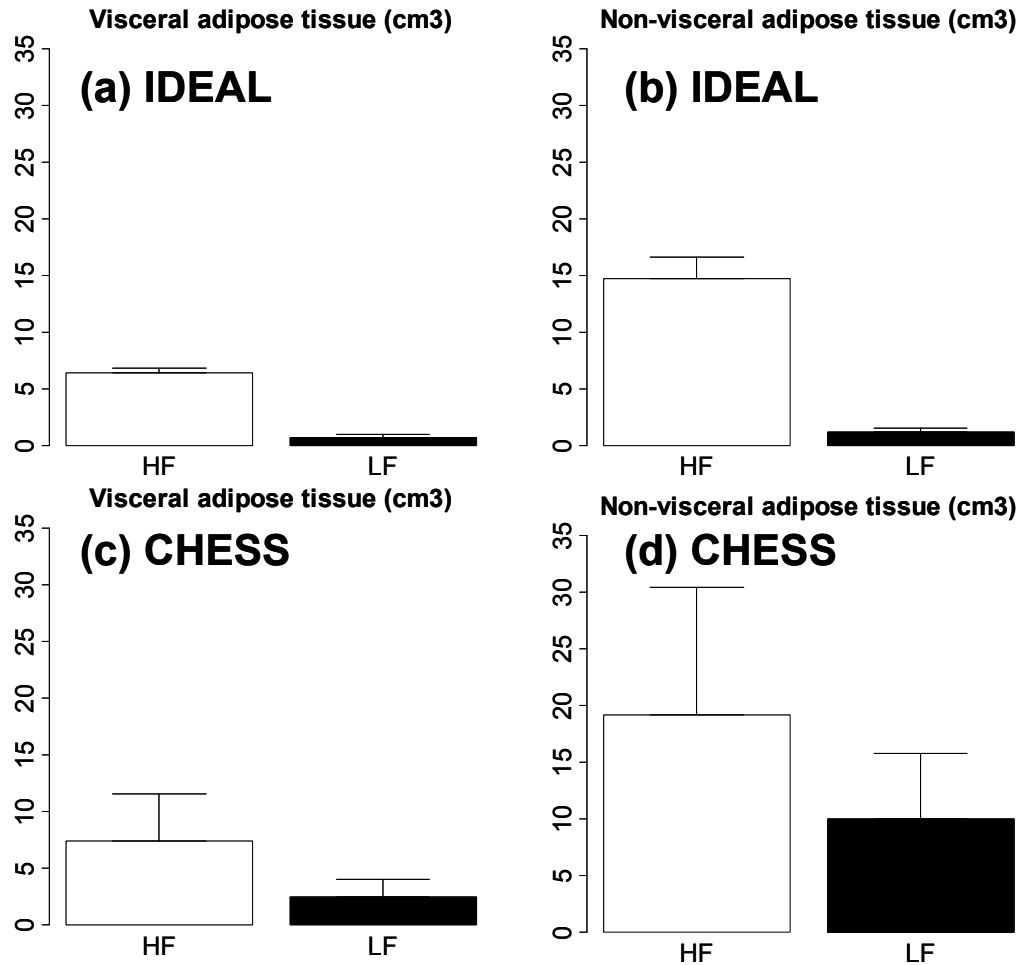
As measured by IDEAL, high fat (HF) diet mice have significantly increased visceral (a) and non-visceral adipose tissue depots (b) as compared to low fat (LF) diet mice (P<0.001). Adipose tissue volume measurements are inflated from the CHESS imaging due to failure of water suppression (c), (d). CHESS measurements of visceral depots are increased (P=0.02) but non-visceral depots are not increased (P>0.10) in high fat diet mice vs. low fat diet mice.

In contrast, CHESS imaging was far less reliable in measuring tissue volumes. As measured by CHESS imaging, visceral adipose tissue volumes were increased 3 fold in high vs. low fat diet mice, 7.4 ± 4.2 cm^3 vs. 2.5 ± 1.5 cm^3, respectively (P=0.02, Figure 4-8-c). As measured by CHESS imaging, non-visceral adipose tissue volumes were not significantly increased in high vs. low fat diet mice, 19.1 ± 11.3 cm^3 vs. 10.0 ± 5.7 cm^3, respectively (P>0.10, Figure 4-8-d).

Liver fat concentration as measured by the chemical assay was compared with visceral adipose tissue volumes and concentration (Figure 4-9). Mice on the high fat diet had both significantly increased visceral adipose tissue volume and also liver fat concentration (P<0.05, Figure 4-9-a). However, fat concentration in visceral adipose tissue did not appear to correlate with liver fat concentration (ρ = -0.48, Figure 4-9-b).

Figure 4-9. Liver Fat Concentration vs. Visceral Adipose Tissue
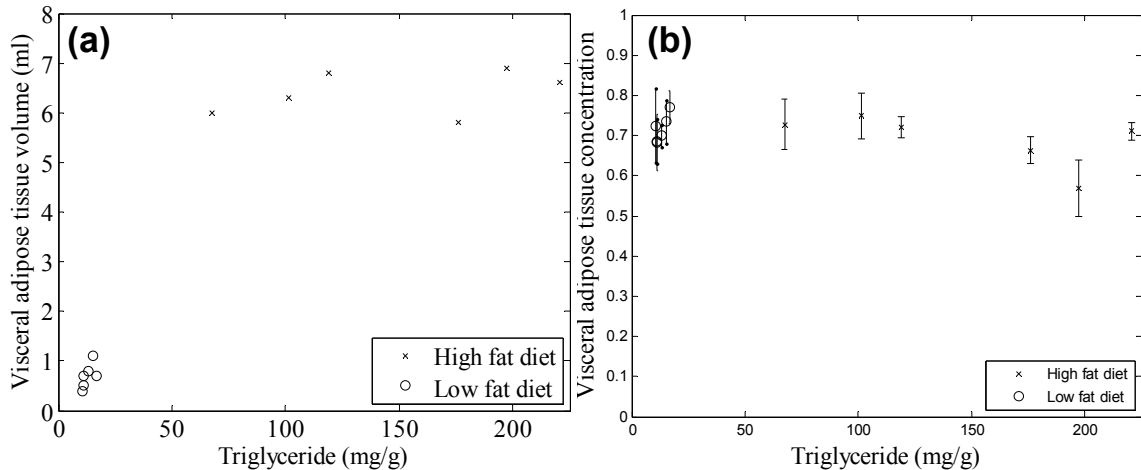
Visceral adipose tissue volume and liver fat triglyceride concentration are both significantly increased due to the high fat diet (P<0.05, a). The IDEAL fat concentration in visceral adipose tissue does not appear to be strongly correlated with liver fat triglyceride concentration (ρ = -0.48) (b).

4.4   Discussion

A robust IDEAL imaging technique for 7T mouse imaging was developed and validated using the IDEAL framework. Ratio image measurements were used to quantify adipose tissue volumes and liver fat fractions in the C57BL/6J mouse model of dietary obesity. Phantoms were used to validate the novel T1 and T2 corrections of the ratio image. IDEAL imaging was found to be more robust and superior to CHESS imaging.

In comparison to the method applied at 1.5T and described in Chapter 2, B0 corrections are required for phenotyping mice on a high field scanner. The shimming is not good enough at 7T to allow B0 variations to be neglected, even over a FOV as small as a mouse (<6 cm). CHESS imaging clearly shows multiple failures that cannot be

corrected in post-processing. However, the IDEAL was able to provide robust fat and water estimates even in the presence of large B0 variations, and the ratio images were very robust. In conclusion, this methodology can be used to routinely assess accumulation/depletion of lipid depots in animal models of obesity on a high field scanner.

Chapter 5 Conclusions and Future Work

MRI was demonstrated to be robust and accurate for phenotyping obese rodents. Novel post-processing corrections were developed and on both low and high field scanners. Studies of obese rats and mice were conducted, and MRI phenotypes of lipid accumulation in visceral and subcutaneous adipose tissue and liver were validated with histology and body weight measurements. Yet, there are still opportunities for future work including acquiring faster images, correcting additional MRI artifacts, and conducting much larger studies of drugs, diet, and exercise, as will be argued in this concluding chapter. Concluding remarks and discussion are given after a discussion of potential future work.

5.1 Future Work

5.1.1 Faster Acquisitions with LEENA and IDEAL

There are opportunities to reduce the MRI acquisition time when performing a 3-point IDEAL method or similar experiment. Acquiring three full sets of images at different TEs is expensive in MRI, though this is much more of a burden to human clinical studies than to animal research. One promising technique is the keyhole Dixon, where the first TE image is fully acquired and the second TE image is only partially acquired (54). Perceptually equivalent reconstructed fat and water images were obtained despite a 25%-38% reduction in acquisition time, depending on the ROI chosen inside the body. SNR was decreased corresponding to the theoretical limitations from total

acquisition time, and some ringing artifacts were observed. Developing this technique for rodent studies on a high field scanner will depend on whether SNR can afford to be reduced beyond current levels.

Another promising technique is a 1-point Dixon acquisition with alternating phase encoding lines taken at different TEs, called Lipid Elimination with an Echo-shifting N/2-Ghost Acquisition (LEENA) (91). Parallel imaging reconstruction techniques are used to remove the ghosting artifacts, and a 50% reduction in acquisition time is possible. Developing this method will require using multiple receiver coils, which were not available for the experiments performed in this work.

5.1.2   Faster IDEAL Reconstruction and Per-pixel T2* Correction

Brent's method is only one of a number of possible improvements to the optimization. Implementing a vectorized version of Newton's method appears promising because analytical first and second derivatives with respect to ψ are available for the IDEAL equations. Newton's method typically has the fastest possible convergence among line search algorithms if the starting condition is close enough to the minimum though caveats remain about maintaining brackets and minimum step sizes (88). The challenge will be initializing the minimization routine such that convergence occurs to a minimum and not one of the many maxima in the residuals curve.

T2* decay was not observed using the shifted spin echo scans at 7T because the effective echo times were on the order of 700 μs or less, whereas T2* is at least 5 ms in most pixels. Correcting T2* decay is still possible in principle because IDEAL can estimate an imaginary component to the B0 inhomogeneity if T2* is equal for fat and water are assumed to be equal (50). The imaginary component of ψ is modeled as per Eq.

(5.1), where the real component remains the same as in typical IDEAL reconstruction and the imaginary component reflects an approximated T2* decay.

$$\psi = \gamma \Delta B_0 + \frac{i}{2\pi} \frac{1}{T2^*}$$ (5.1)

An interesting observation can be made and incorporated into the IDEAL reconstruction when the relationship between T2 and T2* is modeled according to Eq. (5.2). Often it is assumed that k=1 so that the decay due to B0 inhomogeneity is modeled as a simple exponential decay.

$$\frac{1}{T2^*} = \frac{1}{T2} + k\gamma \Delta B_0$$ (5.2)

T2 is on the order of 50-60 ms in many tissues, and therefore the first term of Eq. (5.2) is negligible relative to the second term on a high field scanner because $\gamma \Delta B_0$ is on the order of 100s of Hz. The IDEAL reconstruction can be modified to reflect this fact that under these conditions the real and imaginary components of ψ are no longer independent. On a low field system where the first term of Eq. (5.2) is not negligible it might be possible to extract T2 from the difference of the real and imaginary components of ψ.

5.1.3 Large Scale Mouse Study of Obesity Genes

Given that the IDEAL method has been validated in obese mice at 7T, the next logical step is to perform a much larger study. The results presented in Chapter 4 are critical for planning the correct number of mice from a 'bootstrapping' statistical perspective. The method can be used to study lipid accumulation/depletion in adipose tissue and ectopic depots (muscle, liver) as a function of high fat, low sucrose (HFLS)

and low fat, low sucrose (LFLS) diets as well as switching from HFLS to LFLS at 26 weeks. Mice will be BL6 and A/J, a mouse model previously shown to resist obesity. Animals will be scanned six times during their respective diet regimen to determine group differences including the dynamics of accumulation/depletion of lipid depots. Data will be compared to anticipated changes in fasting glucose levels. In an additional, longer term study, we can characterize the development of NAFLD and its progression to NASH in mice on a HFLS diet and mice on HFLS supplemented with either cholesterol or trans fats, both of which have both been demonstrated to lead to NASH in mice. All imaging results will be correlated to histological assessments.

Successful completion of this study will produce a robust and comprehensive suite of MRI assessments of lipid levels in animal models. This will enable many future studies of the role of genes, diet, and drugs on lipid stores, metabolism, and complications such as fatty liver disease.

5.2   Conclusion

Obesity is a very prevalent disease and co-morbidity of other diseases in many Western societies. While the causes appear to be obviously linked to excessive intake of calories in the typical Western diet, there are numerous underlying genetic and societal factors. As described above and in previous chapters, there is a need to accurately identify genes and novel treatments, and rodent models of obesity will be needed to test the effects of diet, drugs, and lifestyle changes. MRI is undoubtedly the best modality available for studying obese rodents, and many important post-processing methods have been developed in this work to enable such studies.

A robust imaging and analysis paradigm was developed using ratio images to enable effective phenotyping of rodent models of obesity. The remarkable homogeneity of ratio images is useful for both segmentation and 3D visualization, and reproducibility is also improved. The simplicity and reproducibility of this technique is promising for large scale studies of body composition in obese rodents influenced by diet, genetics, exercise, and drugs. These techniques are also generally applicable to clinical research studies of obesity where it is becoming important to quantify regional lipid distribution to track the effects of diet and exercise interventions.

A novel technique for reconstructing mouse images on a high field scanner was developed and shown to be robust even in the presence of severe field inhomogeneity. Reconstruction time and incorrect results have hindered the use of Dixon methods in the past, but the new method is fast and robust. Based on IDEAL, vectorized mathematical equations were derived and a commodity graphics card was used to speed up the computations to only half of the running time on a CPU. The speed advantages of using a GPU will become more important as the trend towards higher resolution images continues to produce larger MRI datasets. The number of function evaluations was reduced using Brent's method to correctly solve the IDEAL reconstruction problem, and the propagation of errors throughout the image was eliminated by the new method.

The new method for high field imaging was validated using a mouse model of dietary obesity. Ratio image measurements were used to quantify adipose tissue volumes and liver fat fractions. IDEAL ratio imaging was found to be more robust and superior to CHESS imaging. IDEAL was able to provide robust fat and water estimates even in the presence of large field inhomogeneity. In conclusion, this methodology can be used to

routinely assess accumulation of lipid depots in animal models of obesity on a high field

scanner.

Bibliography

1. K.R. Fontaine, D.T. Redden, C. Wang, A.O. Westfall, D.B. Allison, Years of life lost due to obesity. JAMA 2003:289:187-193.

2. S.J. Olshansky, D.J. Passaro, R.C. Hershow, J. Layden, B.A. Carnes, J. Brody, L. Hayflick, R.N. Butler, D.B. Allison, D.S. Ludwig, A potential decline in life expectancy in the United States in the 21st century. N.Engl.J Med. 2005:352:1138-1145.

3. C. Bouchard, F.E. Johnston Fat Distribution During Growth and Later Health Outcomes.New York, NY: Liss; 1988. 363 p.

4. G.A. Bray, Pathophysiology of obesity. Am J Clin Nutr 1992:55:488S-494S.

5. J.C. Seidell, P. Bjorntorp, L. Sjostrom, R. Sannerstedt, M. Krotkiewski, H. Kvist, Regional distribution of muscle and fat mass in men--new insight into the risk of abdominal obesity using computed tomography. Int.J Obes. 1989:13:289-303.

6. Y. Matsuzawa, I. Shimomura, T. Nakamura, Y. Keno, K. Kotani, K. Tokunaga, Pathophysiology and pathogenesis of visceral fat obesity. Obes Res 1995:3 Suppl 2:187S-194S.

7. H. Yki-Jarvinen, Ectopic fat accumulation: an important cause of insulin resistance in humans. J R.Soc.Med. 2002:95 Suppl 42:39-45.

8. B.H. Goodpaster, F.L. Thaete, J.A. Simoneau, D.E. Kelley, Subcutaneous abdominal fat and thigh muscle composition predict insulin sensitivity independently of visceral fat. Diabetes 1997:46:1579-1585.

9. J.L. Johnson, D.P. Wan, R.J. Koletsky, P. Ernsberger, A new rat model of dietary obesity and hypertension. Obes Res 2005:13:A113-A114.

10. J.B. Singer, A.E. Hill, L.C. Burrage, K.R. Olszens, J. Song, M. Justice, W.E. O'Brien, D.V. Conti, J.S. Witte, E.S. Lander, J.H. Nadeau, Genetic dissection of complex traits with chromosome substitution strains of mice. Science 2004:304:445-448.

11. S.A. Harrison, W. Fecht, E.M. Brunt, B.A. Neuschwander-Tetri, Orlistat for overweight subjects with nonalcoholic steatohepatitis: A randomized, prospective trial. Hepatology 2009:49:80-86.

12. G. Iacobellis, Imaging of visceral adipose tissue: an emerging diagnostic tool and therapeutic target. Curr.Drug Targets.Cardiovasc.Haematol.Disord. 2005:5:345-353.

13. D.J. Goldstein, Beneficial health effects of modest weight loss. Int.J Obes.Relat Metab Disord. 1992:16:397-415.

14. T. Rice, J.P. Despres, E.W. Daw, J. Gagnon, I.B. Borecki, L. Perusse, A.S. Leon, J.S. Skinner, J.H. Wilmore, D.C. Rao, C. Bouchard, Familial resemblance for abdominal visceral fat: the HERITAGE family study. Int.J Obes.Relat Metab Disord. 1997:21:1024-1031.

15. T.A. Pearson, S.N. Blair, S.R. Daniels, R.H. Eckel, J.M. Fair, S.P. Fortmann, B.A. Franklin, L.B. Goldstein, P. Greenland, S.M. Grundy, Y. Hong, N.H. Miller, R.M. Lauer, I.S. Ockene, R.L. Sacco, J.F. Sallis, Jr., S.C. Smith, Jr., N.J. Stone, K.A. Taubert, AHA Guidelines for Primary Prevention of Cardiovascular Disease and Stroke: 2002 Update: Consensus Panel Guide to Comprehensive Risk Reduction for Adult Patients Without Coronary or Other Atherosclerotic Vascular Diseases. American Heart Association Science Advisory and Coordinating Committee. Circulation 2002:106:388-391.

16. S. Virtue, A. Vidal-Puig, It's not how fat you are, it's what you do with it that counts. PLoS.Biol. 2008:6:e237.

17. A. Schaffler, J. Scholmerich, C. Buchler, Mechanisms of disease: adipocytokines and visceral adipose tissue--emerging role in nonalcoholic fatty liver disease. Nat.Clin.Pract.Gastroenterol.Hepatol. 2005:2:273-280.

18. A. Marti, M.J. Moreno-Aliaga, J. Hebebrand, J.A. Martinez, Genes, lifestyles and obesity. Int.J Obes.Relat Metab Disord. 2004:28 Suppl 3:S29-S36.

19. R.J. Loos, C. Bouchard, Obesity--is it a genetic disorder? J Intern.Med. 2003:254:401-425.

20. A.L. Mark, Dietary therapy for obesity: an emperor with no clothes. Hypertension 2008:51:1426-1434.

21. D.H. Johnson, C.A. Flask, D.P. Wan, P.R. Ernsberger, D.L. Wilson. Quantification of adipose tissue in a rodent model of obesity. Proc SPIE 2006:6143: 2-11.

22. M. Ishikawa, K. Koga, Measurement of abdominal fat by magnetic resonance imaging of OLETF rats, an animal model of NIDDM. Magnetic Resonance Imaging 1998:16:45-53.

23. H. Tang, J.R. Vasselli, E.X. Wu, C.N. Boozer, D. Gallagher, High-resolution magnetic resonance imaging tracks changes in organ and tissue mass in obese and aging rats. American journal of physiology.Regulatory, integrative and comparative physiology. 2002:282:R890-R899.

24. H.Y. Tang, J. Vasselli, E. Wu, D. Gallagher, In vivo determination of body composition of rats using magnetic resonance imaging. In Vivo Body Composition Studies 2000:904:32-41.

25. H. Tang, J.R. Vasselli, E.X. Wu, C.N. Boozer, D. Gallagher, High-resolution magnetic resonance imaging tracks changes in organ and tissue mass in obese and aging rats. Am J Physiol Regul.Integr.Comp Physiol 2002:282:R890-R899.

26. M.A. Gonzalez Ballester, A.P. Zisserman, M. Brady, Estimation of the partial volume effect in MRI. Med.Image Anal. 2002:6:389-405.

27. M. Rebuffe-Scrive, R. Surwit, M. Feinglos, C. Kuhn, J. Rodin, Regional fat distribution and metabolism in a new mouse model (C57BL/6J) of non-insulin-dependent diabetes mellitus. Metabolism, Clinical and Experimental 1993:42:1405-1409.

28. H. Masuzaki, J. Paterson, H. Shinyama, N. Morton, J. Mullins, J. Seckl, J. Flier, A Transgenic Model of Visceral Obesity and the Metabolic Syndrome. Science 2001:294:2166-2170.

29. P.R. Ernsberger, R.J. Koletsky, J.E. Friedman, Molecular pathology in the obese spontaneous hypertensive Koletsky rat: a model of syndrome X. Ann.N.Y.Acad.Sci. 1999:892:272-288.

30. T.H. Ehrich, T. Hrbek, J.P. Kenney-Hunt, L.S. Pletscher, B. Wang, C.F. Semenkovich, J.M. Cheverud, Fine-mapping gene-by-diet interactions on chromosome 13 in a LG/J x SM/J murine model of obesity. Diabetes 2005:54:1863-1872.

31. E. Brakenhielm, R. Cao, B. Gao, B. Angelin, B. Cannon, P. Parini, Y. Cao, Angiogenesis inhibitor, TNP-470, prevents diet-induced and genetic obesity in mice. Circ.Res 2004:94:1579-1588.

32. J. Moitra, M.M. Mason, M. Olive, D. Krylov, O. Gavrilova, B. Marcus-Samuels, L. Feigenbaum, E. Lee, T. Aoyama, M. Eckhaus, M.L. Reitman, C. Vinson, Life without white fat: a transgenic mouse. Genes Dev. 1998:12:3168-3181.

33. M. Korach-Andre, J. Gao, J.S. Gounarides, R. Deacon, A. Islam, D. Laurent, Relationship between visceral adiposity and intramyocellular lipid content in two rat models of insulin resistance. Am J Physiol Endocrinol.Metab 2005:288:E106-E116.

34. S.B. Heymsfield, Z. Wang, T. Lohman, S. Going Human Body Composition. Human Kinetics; 2005. 522 p.

35. I. Janssen, P.T. Katzmarzyk, R. Ross, A.S. Leon, J.S. Skinner, D.C. Rao, J.H. Wilmore, T. Rankinen, C. Bouchard, Fitness Alters the Associations of BMI and Waist Circumference with Total and Abdominal Fat. Obes Res 2004:12:525-537.

36. W. Shen, Z. Wang, M. Punyanita, J. Lei, A. Sinav, J.G. Kral, C. Imielinska, R. Ross, S.B. Heymsfield, Adipose tissue quantification by imaging methods: a proposed classification. Obes Res 2003:11:5-16.

37. R. Ross, L. Leger, R. Guardo, G.J. De, B.G. Pike, Adipose tissue volume measured by magnetic resonance imaging and computerized tomography in rats. J Appl.Physiol 1991:70:2164-2172.

38. A.E. Pontiroli, P. Pizzocri, M. Giacomelli, M. Marchi, P. Vedani, E. Cucchi, C. Orena, F. Folli, M. Paganelli, G. Ferla, Ultrasound measurement of visceral and subcutaneous fat in morbidly obese patients before and after laparoscopic adjustable gastric banding: comparison with computerized tomography and with anthropometric measurements. Obes.Surg. 2002:12:648-651.

39. F.S. Foster, M.Y. Zhang, Y.Q. Zhou, G. Liu, J. Mehi, E. Cherin, K.A. Harasiewicz, B.G. Starkoski, L. Zan, D.A. Knapik, S.L. Adamson, A new ultrasound instrument for in vivo microimaging of mice. Ultrasound Med.Biol. 2002:28:1165-1172.

40. R. Ross, Magnetic resonance imaging provides new insights into the characterization of adipose and lean tissue distribution. Can.J Physiol Pharmacol. 1996:74:778-785.

41. E.M. Delfaut, J. Beltran, G. Johnson, J. Rousseau, X. Marchandise, A. Cotten, Fat suppression in MR imaging: techniques and pitfalls. RadioGraphics 1999:19:373-382.

42. C.S. Poon, J. Szumowski, D.B. Plewes, P. Ashby, R.M. Henkelman, Fat/water quantitation and differential relaxation time measurement using chemical shift imaging technique. Magnetic Resonance Imaging 1989:7:369-382.

43. A. Haase, J. Frahm, W. Hanicke, D. Matthaei, 1H NMR chemical shift selective (CHESS) imaging. Physics in Medicine and Biology 1985:30:341-344.

44. W.T. Dixon, Simple proton spectroscopic imaging. Radiology 1984:153:189-194.

45. G.H. Glover, Multipoint Dixon technique for water and fat proton and susceptibility imaging. J Magn Reson Imaging 1991:1:521-530.

46. S.B. Reeder, Z. Wen, H. Yu, A.R. Pineda, G.E. Gold, M. Markl, N.J. Pelc, Multicoil Dixon chemical species separation with an iterative least-squares estimation method. Magn Reson Med 2004:51:35-45.

47. S.B. Reeder, A.R. Pineda, Z. Wen, A. Shimakawa, H. Yu, J.H. Brittain, G.E. Gold, C.H. Beaulieu, N.J. Pelc, Iterative decomposition of water and fat with echo asymmetry and least-squares estimation (IDEAL): application with fast spin-echo imaging. Magn Reson Med 2005:54:636-644.

48. H. Yu, S.B. Reeder, A. Shimakawa, J.H. Brittain, N.J. Pelc, Field map estimation with a region growing scheme for iterative 3-point water-fat decomposition. Magn Reson Med 2005:54:1032-1039.

49. C.Y. Liu, C.A. McKenzie, H. Yu, J.H. Brittain, S.B. Reeder, Fat quantification with IDEAL gradient echo imaging: correction of bias from T(1) and noise. Magn Reson Med 2007:58:354-364.

50. H. Yu, C.A. McKenzie, A. Shimakawa, A.T. Vu, A.C. Brau, P.J. Beatty, A.R. Pineda, J.H. Brittain, S.B. Reeder, Multiecho reconstruction for simultaneous water-fat decomposition and T2* estimation. J Magn Reson Imaging 2007:26:1153-1161.

51. W. Lu, B.A. Hargreaves, Multiresolution field map estimation using golden section search for water-fat separation. Magn Reson Med 2008:60:236-244.

52. X. Zhang, M. Tengowski, L. Fasulo, S. Botts, S.A. Suddarth, G.A. Johnson, Measurement of fat/water ratios in rat liver using 3D three-point dixon MRI. Magn Reson Med 2004:51:697-702.

53. C.A. Flask, B. Dale, J.S. Lewin, J.L. Duerk, Radial alternating TE sequence for faster fat suppression. Magn Reson Med 2003:50:1095-1099.

54. C.A. Flask, K.A. Salem, H. Moriguchi, J.S. Lewin, D.L. Wilson, J.L. Duerk, Keyhole Dixon method for faster, perceptually equivalent fat suppression. J Magn Reson Imaging 2003:18:103-112.

55. B.D. Coombs, J. Szumowski, W. Coshow, Two-point Dixon technique for water-fat signal decomposition with B0 inhomogeneity correction. Magn Reson Med 1997:38:884-889.

56. J. Ma, Dixon techniques for water and fat imaging. J.Magn Reson.Imaging 2008:28:543-558.

57. D. Hernando, J.P. Haldar, B.P. Sutton, J. Ma, P. Kellman, Z.P. Liang, Joint estimation of water/fat images and field inhomogeneity map. Magn Reson.Med. 2008:59:571-580.

58. M.S. Hansen, D. Atkinson, T.S. Sorensen, Cartesian SENSE and k-t SENSE reconstruction using commodity graphics hardware. Magn Reson Med 2008:59:463-468.

59. Stone, Accelerating advanced MRI reconstructions on GPUs. Journal of Parallel and Distributed Computing 2008:68:1307.

60. E. Lunati, P. Marzola, E. Nicolato, M. Fedrigo, M. Villa, A. Sbarbati, In vivo quantitative lipidic map of brown adipose tissue by chemical shift imaging at 4.7 tesla. J.Lipid Res. 1999:40:1395-1400.

61. E.M. Haacke, R.W. Brown, M.R. Thompson, R. Venkatesan. Water/Fat Separation Techniques. In: E. M. Haacke, R. W. Brown, M. R. Thompson, and R. Venkatesan

(Eds.), editors. Magnetic resonance imaging : physical principles and sequence design. New York: John Wiley & Sons, Inc.; 1999. pp. 421-449.

62. S Koletsky. New type of spontaneously hypertensive rats with hyperlipemia and endocrine gland defects. In: K. Okatomo (Ed.), editors. Spontaneous Hypertension: Its Pathogenesis and Complications. Tokyo, Japan: Igaku Shoin Ltd.; 1972. pp. 194-197.

63. S.M. Grundy, Small LDL, atherogenic dyslipidemia, and the metabolic syndrome. Circulation 1997:95:1-4.

64. D.P. Wan, D.H. Johnson, J.L. Johnson, R.J. Koletsky, C. Flask, P. Ernsberger. Magnetic Resonance Imaging of Visceral and Subcutaneous Fat Distribution in Genetic Versus Dietary Obesity. NAASO, The Obesity Society, 2005 National Meeting 10-19-2005:13: A172-A174.

65. G. Iacobellis, Imaging of visceral adipose tissue: an emerging diagnostic tool and therapeutic target. Current drug targets - Cardiovascular & haematological disorders 2005:5:345-353.

66. L.R. Dice, Measures of the Amount of Ecologic Association Between Species. Ecology 1945:26:297-302.

67. J.J. Bartko, Measurement and reliability: statistical thinking considerations. Schizophr.Bull. 1991:17:483-489.

68. R Development Core Team R: A language and environment for statistical computing.Vienna, Austria: R Foundation for Statistical Computing; 2005.

69. O. Salvado, D.L. Wilson, Removal of local and biased global maxima in intensity-based registration. Med.Image Anal. 2007:11:183-196.

70. D. Kahaner, C. Moler, S. Nash Numerical methods and software.Upper Saddle River, NJ, USA: Prentice-Hall, Inc.; 1989. 495 p.

71. D. Gallagher, D. Belmonte, P. Deurenberg, Z. Wang, N. Krasnow, F.X. Pi-Sunyer, S.B. Heymsfield, Organ-tissue mass measurement allows modeling of REE and metabolically active tissue mass. Am J Physiol 1998:275:E249-E258.

72. A.C. Westphalen, A. Qayyum, B.M. Yeh, R.B. Merriman, J.A. Lee, A. Lamba, Y. Lu, F.V. Coakley, Liver fat: effect of hepatic iron deposition on evaluation with opposed-phase MR imaging. Radiology 2007:242:450-455.

73. P.A. Hardy, R.S. Hinks, J.A. Tkach, Separation of fat and water in fast spin-echo MR imaging with the three-point Dixon technique. J Magn Reson Imaging 1995:5:181-185.

74. O. Salvado, C. Hillenbrand, S. Zhang, D.L. Wilson, Method to correct intensity inhomogeneity in MR images for atherosclerosis characterization. IEEE Trans.Med.Imaging 2006:25:539-552.

75. J.G. Sled, A.P. Zijdenbos, A.C. Evans, A nonparametric method for automatic correction of intensity nonuniformity in MRI data. IEEE Trans.Med.Imaging 1998:17:87-97.

76. K.K. Changani, A. Nicholson, A. White, J.K. Latcham, D.G. Reid, J.C. Clapham, A longitudinal magnetic resonance imaging (MRI) study of differences in abdominal fat distribution between normal mice, and lean overexpressors of mitochondrial uncoupling protein-3 (UCP-3). Diabetes, Obesity and Metabolism 2003:5:99-105.

77. F. Schick, J. Machann, K. Brechtel, A. Strempfer, B. Klumpp, D. Stein, S. Jacob, MRI of muscular fat. Magnetic Resonance in Medicine 2002:47:720-727.

78. J. Machann, O.P. Bachmann, K. Brechtel, D.B. Dahl, B. Wietek, B. Klumpp, H.U. H,,ring, C.D. Claussen, S. Jacob, F. Schick, Lipid content in the musculature of the lower leg assessed by fat selective MRI: Intra- and interindividual differences and correlation with anthropometric and metabolic data. J Magn Reson Imaging 2003:17:350-357.

79. J.P. Despres, S. Moorjani, P.J. Lupien, A. Tremblay, A. Nadeau, C. Bouchard, Regional distribution of body fat, plasma lipoproteins, and cardiovascular disease. Arteriosclerosis 1990:10:497-511.

80. M.K. Tulloch-Reid, R.L. Hanson, N.G. Sebring, J.C. Reynolds, A. Premkumar, D.J. Genovese, A.E. Sumner, Both subcutaneous and visceral adipose tissue correlate highly with insulin resistance in african americans. Obes Res 2004:12:1352-1359.

81. R.N. Bergman, S.P. Kim, K.J. Catalano, I.R. Hsu, J.D. Chiu, M. Kabir, K. Hucking, M. Ader, Why visceral fat is bad: mechanisms of the metabolic syndrome. Obes Res 2006:14 Suppl 1:16S-19S.

82. O. Salvado, C.M. Hillenbrand, D.L. Wilson, Partial volume reduction by interpolation with reverse diffusion. International Journal of Biomedical Imaging 2006:2006:1-13.

83. T. Namimoto, Y. Yamashita, K. Mitsuzaki, Y. Nakayama, O. Makita, M. Kadota, M. Takahashi, Adrenal masses: quantification of fat content with double-echo chemical shift in-phase and opposed-phase FLASH MR images for differentiation of adrenal adenomas. Radiology 2001:218:642-646.

84. G. Brix, S. Heiland, M.E. Bellemann, T. Koch, W.J. Lorenz, MR imaging of fat-containing tissues: valuation of two quantitative imaging techniques in comparison with localized proton spectroscopy. Magn Reson Imaging 1993:11:977-991.

85. H.K. Hussain, T.L. Chenevert, F.J. Londy, V. Gulani, S.D. Swanson, B.J. McKenna, H.D. Appelman, S. Adusumilli, J.K. Greenson, H.S. Conjeevaram, Hepatic fat fraction: MR imaging for quantitative measurement and display--early experience. Radiology 2005:237:1048-1055.

86. L. Calderan, P. Marzola, E. Nicolato, P.F. Fabene, C. Milanese, P. Bernardi, A. Giordano, S. Cinti, A. Sbarbati, In vivo phenotyping of the ob/ob mouse by magnetic resonance imaging and 1H-magnetic resonance spectroscopy. Obes Res 2006:14:405-414.

87. J.M. Chan, E.B. Rimm, G.A. Colditz, M.J. Stampfer, W.C. Willett, Obesity, fat distribution, and weight gain as risk factors for clinical diabetes in men. Diabetes Care 1994:17:961-969.

88. W.H. Press, S.K. Teukolsky, W.T. Vetterling, B.P. Flannery. Minimization or Maximization of Functions. In: W. H. Press, S. K. Teukolsky, W. T. Vetterling, and B. P. Flannery (Eds.), editors. Numerical Recipes in C: the Art of Scientific Computing. Cambridge: Cambridge University Press; 1992. pp. 394-455.

89. M. Jacob, B.P. Sutton, Algebraic Decomposition of Fat and Water in MRI. Medical Imaging, IEEE Transactions on 2009:28:173-184.

90. D.H. Johnson, C.A. Flask, P.R. Ernsberger, W.C. Wong, D.L. Wilson, Reproducible MRI measurement of adipose tissue volumes in genetic and dietary rodent obesity models. J Magn Reson Imaging 2008:28:915-927.

91. C. Flask, J. Lewin, J.L. Duerk. **Lipid Elimination with an Echo-shifting N/2-Ghost Acquisition (LEENA)**. Proc.12th Annual Meeting of ISMRM 2004: 269.